Image analysis for morphology, rheology and degradation study of railway ballast
A review

Guo, Yunlong; Markine, Valeri; Zhang, Xuehui; Qiang, Weile; Jing, Guoquig

DOI
10.1016/j.trgeo.2018.12.001

Publication date
2019

Document Version
Accepted author manuscript

Published in
Transportation Geotechnics

Citation (APA)
Guo, Y., Markine, V., Zhang, X., Qiang, W., & Jing, G. (2019). Image analysis for morphology, rheology and degradation study of railway ballast: A review. *Transportation Geotechnics*, *18*, 173-211. https://doi.org/10.1016/j.trgeo.2018.12.001

Image analysis for morphology, rheology and degradation study of railway ballast: A review

Yunlong Guo[1], Valeri Markine[1], Xuehui Zhang[1], Weile Qiang[2], Guoqing Jing[2 *]

1. Faculty of Civil Engineering and Geosciences, Delft University of Technology, Delft, 2628CN, Netherlands

2. School of Civil Engineering, Beijing Jiaotong University, Beijing, 100044, China

** Corresponding author*

Email addresses: gqjing@bjtu.edu.cn; yunlongguo@tudelft.nl

Abstract: The performance and deformation of ballast bed are significantly influenced by the particle morphology (size and shape), the rheology (translation and rotation), and the degradation (breakage and abrasion). Regarding the ballast particle morphology, the ballast particle size is generally measured by sieving and described with the Particle Size Distribution (PSD), while the particle shape is normally classified as three characteristics, the form, angularity, and surface texture. Quantifying particle morphology with current manual methods is difficult to obtain accurate results (often subjective).

Concerning the ballast particle rheology, almost all the related studies are based on numerical simulations, e.g. the Discrete Element Method (DEM). A limited number of studies were performed to record the translation and rotation with the electronic devices embedded in ballast layer. However, the numerical simulations can only precisely reflect the ballast particle rheology in quasi-static tests (e.g. direct shear test), and the electronic devices can only record the ballast particle rheology in the limited areas, where they were placed.

The ballast breakage could be evaluated by the change of the PSD, but the determination of PSD involves significant errors. Additionally, the manual methods could not fully quantify the ballast abrasion. As a result, more accurate evaluation methods need to be developed and utilised for the validation and confirmation of the degradation-related studies.

Towards these limitations, the studies on two-dimensional (2D) and three-dimensional (3D) image analysis methods for granular materials are reviewed, discussing their existing and potential utilisation in railway ballast applications. This paper can be of interest to the researchers, who are dealing with the performance and deformation of ballast bed. Additionally, a special attention can be paid to utilising the image analysis for accurate particle morphology quantification, particle rheology investigation and ballast degradation evaluation.

Keywords: Ballast; Image analysis; Morphology; Rheology; Degradation; X-ray; PIV

1 Introduction

Ballast particles, uniformly graded crushed rocks, are one of the most fundamental components in railway tracks. They are placed between and under the sleepers to form the ballast track. Furthermore, the presence of ballast particles in railway tracks help keep the track in the required position, transfer the loads to the subgrade, as well as provide sufficient drainage. To guarantee the critical performance of ballast bed, the ballast particle properties, such as the parent rock type, particle size and shape, etc. should be well assessed. Usually, the material of the parent rock is analysed using the petrographic methods, and other important properties, such as, the particle size distribution (PSD) and the percentage of the flaky or elongated particles are tested as well. Although the ballast particles are carefully tested, they still need more comprehensive and reliable tests, which is necessary for the increasing demand of the higher train speed, the heavier axle load and the larger operation intensity. Most importantly, the increasing usage of ballast tracks leads to unacceptable deformation and poor (fast degraded) performance of the ballast bed, which directly affect the maintenance frequency and the lifespan of ballast track [1].

To solve these issues, more emphasis should be put on studying the effect factors affecting the performance and deformation of ballast bed. The performance and deformation of ballast bed are significantly influenced by the ballast particle morphology (size and shape), the rheology (translation and rotation), and the degradation (breakage and abrasion). Besides, the ballast deformation is mostly affected by three primary mechanisms: densification, distortion, and degradation [2]. The densification can be described as the change of shape and compressibility of the ballast particles; the distortion is defined by the rheology (translation and rotation) of individual ballast particles; and the degradation is controlled by the two main processes, namely, breakage and abrasion. Generally, the performance includes durability, shear strength, stiffness and resilience. In a number of studies, it was shown that the high performance of ballast particles mainly consists of the following factors [3]:

- hardness and durability of the particles,
- high density and low water absorption of the particle material,
- reasonable PSD of the ballast particles,
- presence of angular particles,
- limited percentage of flaky or elongated particles,
- presence of the rough particles with fresh fracture surface.

Obviously, most of the listed characteristics are related to the ballast particle morphology. Similar conclusions can be found in the studies on other granular materials, such as, sands, asphalt mixtures, rock-fill and concrete [4-6]. Therefore, the ballast particle morphology, rheology, and degradation are the three key factors determining the performance and deformation of ballast bed.

However, most of the studies on these three factors have some limitations and drawbacks, such as the rough indices for particle morphology evaluation, the types of ballast degradation etc. The image analysis is the more cutting-edge and rapidly developing one. The image analysis is used to analyse the 2D images (photography, particle projection) or recorded videos of the particles. Alternatively, it can also be used to analyse the 3D images obtained through laser scanning, recombination of pictures from different viewpoints, or cone beam X-ray tomography.

The limitations and drawbacks of the traditional methods for these three factors are introduced in the following three sub-sections, the 1.1, 1.2, and 1.3 respectively. Afterwards, the image analysis methods for these three factors are presented in the three sections, the Section 2 (Morphology) and Section 3 (Rheology).

1.1 Morphology

Evaluating the particle morphology more accurately and efficiently is necessary for studying its correlation with the performance and deformation of ballast bed [2, 7]. The particle morphology includes the particle size and the particle shape. The size of ballast particles is usually determined using the sieving and expressed in the PSD, while the shape is normally evaluated roughly with the aspect ratio of the particles [8]. More importantly, because of the rough particle morphology evaluation, the evidence of its effects on the performance and deformation of ballast particles is inconclusive.

For instance, the size is traditionally based upon the sieve analysis, and presented as the PSD curve, however, that is a rough evaluation. Because the ballast particles are irregular compared to simple spheres, specifically, one ballast particle can have plenty of different dimensions. Even though the particles pass through the sieve that cannot accurately measure the size of the particles and only presents the smallest particle projection can go through the sieve mesh. Furthermore, the final separation results of the particles mainly rely on the sieving duration, which means longer time sieving can increase the passing possibility by making the particles rotate more to fit the sieve mesh [9]. Even though measuring the particle size one by one is more precise, it is time-consuming and with large personal errors. For example, to obtain the three main dimensions of the individual ballast particles, the proportional calliper is often used. The length and the height are easy to measure with this device, but measuring the width is complicated and its result depends on the experience of the measuring person in most cases.

Because of the rough particle size evaluation, the evidence of particle size or the PSD effects on ballast performance is still inconclusive. Such as in [10], it is reported that particle size has little influence on shear strength, however, in other studies [11, 12] it is shown that the shear strength can increase or decrease as the particle size increases. Regarding the PSD effect, most researchers believe that a narrower PSD can provide better ballast performance, while some researchers argue that ballast assemblies with the mixture of large and small particles that results in wider PSD, can perform better [13].

Currently, in the case of ballast particle shape, the clear standards are still not available, and normally it is evaluated by manual means (often subjective). For instance, the general method for particle shape evaluation [14] is to manually measure the three main dimensions of the particle (length, width, and height), producing the two rough indices, the Flat or Elongated ratio (*FR* or *ER*). They are respectively expressed as the equations in Table 8, at Flat or Elongated ratio (marked with the reference, Fernlund, 2005, 2007). Recently, several morphological indices are proposed, including the Sphericity [15], the Angularity index [16] and the Surface texture index [17], consisting of numerous manual procedures. Therefore, the current particle morphology evaluation methods cause of low efficiency and accuracy, thus in most cases they only produce very rough indices [13].

Because of the rough indices, the earlier studies on the particle shape effects on the performance of ballast layers did not always reach a consensus. For example, it is found that ballast specimens with flaky or elongated particles can cause lower resilience [13]. However, a limited percentage of flaky or elongated particles leads to higher shear strength and thus a lower rate of settlement accumulation [12]. Nevertheless, it is reported that adding flaky or elongated particles results in more severe degradation and higher deformation [18]. That is due to different particle morphology will further differ the compaction of ballast layer, the contact number between ballast particles and the ballast particle degradation etc., which will finally lead to different performance [19, 20].

Accordingly, the accurate and efficient methods for ballast particle morphology evaluation are significant for the further studies (i.e. performance and deformation of ballast bed). The techniques of image analysis have been developed for evaluating the morphology of particles in pavement layer, concrete, and railway ballast bed. As an efficient, accurate and viable solution, it should have further been studied.

1.2 Rheology

Ballast particle rheology is defined as the movement of individual particles, and further the flow of the whole ballast layer, which has the similar definition as the particle rheology in concretes [21]. For the granular level, it has two properties, the particle translation and the particle rotation, while for the entirety level, it can be characterised by the irrecoverable distortion.

Studies on ballast particle rheology should be performed deeper, because according to the studies so far, the performance and deformation of ballast bed are mainly dependent on the ballast particle rheology [22, 23]. For example, track irregular geometry (e.g. hanging sleeper) that is caused by the differential settlement, which results from the different ballast particle rheology at different parts, as well as the corresponding ballast rearrangement and compaction diversity under adjacent sleepers [24]. This can be also proved by using the geosynthetics to restrict the ballast particle rheology for providing better performance and less deformation of ballast layer [1].

For the importance of ballast particle rheology, plenty of studies were performed including numerical simulations (using the DEM), laboratory tests and in-site tests. However, there exist some limitations and drawbacks of these research methods.

Concerning the numerical simulation studies, the DEM is the most widely utilised due to its ability of obtaining the complete particle information (acceleration, velocity, displacement, contact force). Additionally, it can simulate the characteristics of granular materials (density, morphology), and more importantly study the effects of particle breakage and abrasion on the performance (shear strength, resilience) [1]. However, using the DEM has two main limitations, computing time and energy dissipation.

Regarding the computing time, it is not sufficient to study the ballast particle rheology with only a few cyclic loadings, however, more cycles cost more computing time. For instance, in the simulation of cyclic triaxial tests, thousands of particles may be involved in one 3D DEM model, to analyse that costs large amounts of time. This problem becomes more serious when non-spherical particles are modelled for more realistic particle shape [25, 26], e.g. when clumps or clusters are used in the software, Particle Flow Code (PFC) [27-29]. They are generated by adding two or more spheres together to form one particle. There is a difference between the clump (a rigid particle) that cannot break up regardless of the forces loading on it, and the cluster that is crushable due to the component spheres are bonded together by the parallel bonds. The clusters will crush when the force acting on them is over the prescribed value [30]. Although in some other software, the polyhedral particles are utilised with better shapes than spheres, the main possible imperfection is that the applied particles are uncrushable [24]. For instance, in [31], a novel statistical method was proposed to generate virtual 3D particles with realistically complex yet controllable shapes.

When the kinetic energy is not properly dissipated in DEM simulations, the particle movements are larger than real, making the particle rheology unrealistic. The energy dissipation is related to model calibration, which means the energy supplied to the ballast layer is dissipated through the ballast sliding, rolling, breaking and wearing, practically. However, in the DEM models, that is extremely difficult to adjust. For example, in most PFC models of railway ballast, the kinetic energy is dissipated through frictional sliding and local damping [28, 29]. The local damping applies a damping force (magnitude proportional to unbalanced force) to each ball. Mostly, the value of the local damping is taken as 0.7, which means that 70% of the unbalance force between particles is lost after each time interval. Using the local damping is the most appropriate for quasi-static deformation simulations (e.g. direct shear test model [32]). However, when it comes to the dynamic simulation of compact particles (e.g. cyclic triaxial test [33]), only local damping is not sufficient to dissipate the energy. This becomes intensified when the simulation is dominated by rapid impacts (e.g. tamping tine inserting). More explanations about how damping works are shown in [34].

Regarding the laboratory tests for the study on ballast particle rheology, the SmartRock [24] and Sensing stones [35] are the latest technological devices. The SmartRock is a 3D printed particle with an electronic unit embedded inside. The electronic unit is a 9-degree-of-freedom motion/vibration sensor consisting of a triaxial gyroscope, a triaxial accelerometer, and a triaxial magnetometer, which records rotation, translation, and orientation, respectively. The Sensing stones are piezoelectric-type triaxial acceleration sensors, simultaneously measuring the acceleration in three directions. Therefore, the SmartRock can record real-time ballast particle rheology, including translation and rotation, but it can only record the rheology of the positions, where the SmartRock was placed. Moreover, when the particle rheology of every individual particles needs to be studied, this technological device seems insufficient. The other technological device, the Sensing stones can measure all the vibrations actuating in the ballast layer, however, it has the same limitation as the SmartRock.

The above discussions demonstrate that cutting-edge methods are needed for the study on ballast particle rheology. The image analysis methods can be an effective solution for that, because they can accurately record the initial and final information (e.g. position) of every individual particle. Moreover, among the image analysis methods, the Particle Image Velocimetry (PIV) is already performed in the particle rheology studies of sands and soil. Most importantly, the results of particle rheology can be utilised to calibrate the particle movement in numerical simulations (DEM models). The PIV will be introduced in details in Section 3.

1.3 Degradation

Ballast degradation is another important factor influencing the ballast performance and deformation, including two main types, breakage and abrasion [1]. However, the current evaluation methods for the breakage and abrasion are still insufficient and need improvement. That will affect the test results when ballast degradation frequently occurs and has great influences, such as the shear strength measurement in triaxial tests and the degradation quantification in laboratory tests (e.g. the micro-Deval test). They are discussed in the following paragraphs, furthermore, the limitations and insufficiency of the widely-used degradation evaluation methods are discussed.

Particle breakage significantly influences the performance (e.g. shear strength) and the deformation of any kinds of ballast material [1]. On one hand, particle size would be changed after crushing and generally cause the densification and the contaminations clogging the voids, which may further increase the shear strength [13]. On the other hand, the drainage failure would also induce dramatic ballast settlement. As reported in [36], saturation increased settlement by about 40% of that of dry ballast. Accordingly, the effects of particle breakage on the performance and deformation of ballast bed are complicated, which results from the insufficient breakage evaluation.

For instance, all the breakage evaluation methods are based on sieving, analysing the change of the PSD or the percentage of particles passing some certain sieve size, when performing laboratory tests, e.g., the Los Angeles Abrasion test, the triaxial test, and the prismoidal triaxial test [1, 37]. The breakage index B_g (proposed in [38]) calculates particle sizes between the initial and final particle size distributions. To be more specific, it is the sum of the difference in percentage retained on sieves, having the same sign. However, it may not be sufficient to evaluate ballast breakage only by calculating the PSD, since the final PSD results are obtained based on various types of ballast breakage, including corner breakage, splitting in the middle, and breaking into several parts.

Most of the current methods that can evaluate ballast abrasion are related to the image analysis. For example, in [39], the abrasion is evaluated by the changes of ballast particle morphology. The University of Illinois aggregate image analyser (UIAIA) and a second-generation aggregate imaging system (AIMS) are utilised to capture changes of individual particles before and after the micro-Deval test [39].

Consequently, among the previous methods, image analysis is the most potential and effective one, which can be a significant method to evaluate the ballast degradation. More studies based on that should be performed for better understanding of the ballast degradation mechanism and further its effects on the performance and deformation of ballast bed [1, 40].

This paper reviews the studies on the 2D and 3D image analysis for the morphology, rheology and degradation of granular materials. An overview of image analysis methods is presented, afterwards, their existing and potential utilisations in railway ballast studies are discussed. The images are obtained from various technological means, such as, the laser scanning and the X-ray. In this paper, the various methods are summarised, which will assist future researchers to develop new methods until a more accurate and efficient method is achieved. Moreover, the research gaps and promising research directions of the image analysis for railway ballast are discussed. Gathering all the information into a paper can also offer researchers with a beneficial reference for future work.

The paper is structured as follows. The image analysis methods for the particle morphology are introduced in Section 2. A detailed and critical review of particle degradation studies are highlighted in this section as well, due to the better morphology evaluation leads to a better ballast degradation evaluation. Additionally, this can help analysing the possibility of the morphology evaluation methods to quantify ballast particle degradation. The particle rheology studies (Section 3) are introduced with the PIV emphatically discussed. Finally, the discussions and perspectives of the image analysis for railway ballast studies are given in the last section.

2 Morphology and degradation evaluation

Particle morphology (size and shape) has direct effects on the performance and deformation of the granular material layer, such as, the sands, rock-fills, and asphalt or concrete layers [4-6]. The particle morphology is significant for railway ballast as well [41]. However, the traditional methods are somewhat insufficient for the particle morphology evaluation [9]. For instance, the PSD (for size) and the Flat or Elongated ratio (for shape) are the two main indicators analysed before laboratory tests or railway line construction. The rough quantification of ballast particle morphology normally leads to inconclusive test results and controversial conclusions [13].

Consequently, image analysis methods with advanced technical means have been developed [42, 43]. These methods are more efficient and can provide more accurate particle morphology evaluation and corresponding morphological indices, including:

Size: 1. the Particle size distribution,

2. the Volume & Surface area;

Shape: 3. the form (Flat or Elongated ratio, Sphericity etc.),

4. the angularity (Roundness, Angularity index),

5. the surface texture (Roughness, Surface texture index).

Ballast degradation is another crucial factor that influences the ballast performance and deformation, due to the morphology change during degradation. It generally classified as two main types: breakage and abrasion. Ballast particle breakage has significant influences on the shear strength and the deformation of any kinds of ballast material, which consequently affects the track stability [13]. The ballast particle abrasion is another important type of ballast degradation, and it is demonstrated in [44] that permanent settlement is related to the ballast abrasion. However, few studies concern the degradation evaluation methods, and most studies utilised only rough evaluation indices, e.g. indices from the PSD comparison, causing inaccurate results. Therefore, it is vital to develop an evaluation method before studying the relationship between ballast degradation and the degradation-related performance or deformation.

In this section, the image analysis methods for particle morphology evaluation are introduced in details. It should be noted that these methods for granular materials are already or potentially used for the railway ballast application. This will help analysts and engineers select an appropriate image analysis method and a suitable technical mean, when performing laboratory/in-site ballast tests or building a railway line. Moreover, all the technical means have the advantages and disadvantages, therefore, analysing and comparing them is helpful to know where to improve the technical means. Most importantly, introducing the image analysis methods will assist future researchers to improve existing morphology evaluation methods. Moreover, using the image analysis, the degradation evaluation methods for granular materials are introduced as well. Most of them rely on the morphological indices from the morphology evaluation. In other words, they mostly measure the 2D particle morphology change (size, form, angularity, surface texture) of the whole testing sample. Particularly, cutting-edge 3D degradation evaluation methods for individual particles are introduced, providing promising image analysis methods for ballast degradation evaluation.

2.1 Particle morphology evaluation with image analysis

2.1.1 Shape and size evaluation

The particle shape can be described with various kinds of characteristics. Among them, the most widely-accepted one includes the form, the angularity, and the surface texture, as shown in Figure 1. The three shape characteristics are defined based on the different scales. According to [45], they are utilised to characterise particle shape, because each of shape characteristics is independent and can be different without influencing the other two characteristics.

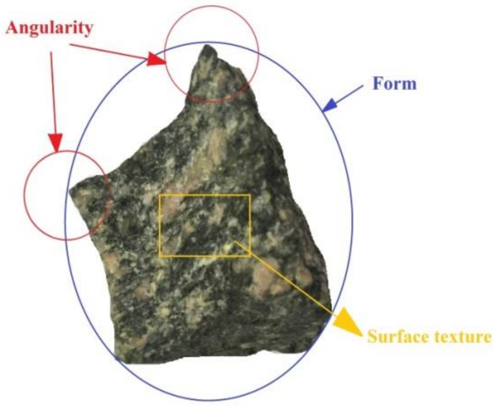

Figure 1 Shape characteristics of ballast particle (reproduced from [20])

Therefore, the particle shape is mostly evaluated by quantifying the three shape characteristics. The form, as the large scale, is mainly quantified with the morphological indices, e.g. the Flat or Elongated ratio [20, 46] and the Sphericity [15, 47-49]. Some other morphological indices are also proposed in some studies, e.g. the Ellipsoidness [50] and the Form index [43, 51-53]. The angularity is quantified with the morphological indices, e.g. the Angularity index and Roundness [42, 43, 53-55], and the Roughness (Surface texture index) is used for the surface texture evaluation [42, 43, 51, 56].

In the reviewed references, the applied apparatuses, image acquisition methods (raw data), the study highlights and the output (morphology indices) are given in Table 3, Table 4, Table 5, Table 6 and Table 7, and the corresponding calculation methods of the morphological indices for the shape quantification are summarised in Table 8, Table 9 and Table 10.

The particle size is traditionally evaluated by the Particle Size Distribution (PSD), which is the curve presenting the mass percentage that can pass some certain sieve sizes. More accurately, the PSD can be obtained by measuring all the particle sizes of one sample with image analysis methods. The three axes of a particle can be measured and one of them can be used as the particle size. Moreover, the particle volume or surface area can also reflect the particle size. The image analysis methods for size evaluation are combined with the shape evaluation, given in the Table 3, Table 4, Table 5 and Table 7, and the corresponding calculation methods are given in Table 11.

It should be noted that the morphological indices almost cover all the popular indices utilized for particle morphology evaluation. By doing this can help researchers compare the calculation methods and find the morphological indices that are suitable for their research. Moreover, analysing the development tendency of these indices will also assist to find insufficient points that need improvement. These morphological indices are categorized based on the techniques that are utilised for particle shape acquisition, i.e. manual measurement and image analysis.

The techniques for the manual measurement use some less accuracy devices (e.g. convexity gage and sliding rod caliper). Based on the measured values (e.g. perimeter and area of particle projection), many morphological indices for particle shape evaluation are proposed, as shown in Table 8, Table 9, and Table 10 (marked with "Manual measurement"). It should be noted that some calculation methods of these morphological indices are also used for image analysis in some studies, because they can be accurate when the needed parameters (e.g. particle volume and surface area) are precisely measured with image analysis methods. Examples can be found in the Table 8-12, such as the Circularity and the Sphericity (Hyperlink), whose reference, description and the utilised equations are given in Table 8, marked with the "Riley, 1941".

In recent decades, the techniques for particle image acquisition and analysis are rapidly developing. Compared with the traditional means, the particle morphology evaluation with image analysis methods is more accurate and objective. Image analysis methods analyse 2D or 3D images that are acquired with various technical means (apparatus), such as, photography (camera), X-ray (computed tomography scanner), 3D imaging (3D scanner) and laser scanning (laser scanner), etc. Various technical means with different apparatus significantly influence the precision of the images, thus the results of particle morphology evaluation. Photography utilises cameras to take particle photos, and in most cases the photos are converted into binary images. X-ray can take photos at different cross sections of particles, and the cross sections of which can be used to form the 3D image for the same particle. 3D imaging utilises the particle pictures from different views to form the 3D image. Laser scanners collect the relative positions (coordinates) of the surface points and subsequently the 3D image is formed by the triangle meshes (by connecting every three adjoint points).

The image analysis methods are categorized as the Static Image Analysis (SIA) and the Dynamic Image Analysis (DIA). This categorisation is according to whether particles are moving during the image capture. The SIA utilises cameras to capture images of particles lying down on a flat plate/belt, while the DIA captures images of particles falling from a conveyer belt. The image analysis methods and the corresponding morphological indices (SIA, DIA) will be introduced in the two following sub-sections.

2.1.1.1 Static Image Analysis

In this sub-section, the SIA methods are introduced, and they are classified in the following aspects. The classification is according to the image acquisition methods.

- the Photography analysis with 2D output (Table 3),
- the Photography analysis with 3D output (Table 4),
- the image analysis systems (Table 5)
- and others (Table 6).

The Photography analysis utilises 2D digital images or projections of particles (i.e. particle outline), which are obtained with cameras or projectors, respectively. The Photograph analysis outputs have two types, the 2D and the 3D, which are given in the Table 3 and Table 4, respectively. The image analysis systems for particle morphology evaluation (introduced in Table 5) include the Aggregate Image Measurement System (AIMS), University of Illinois Aggregate Image Analyzer (UIAIA), Laser-Based Aggregate Scanning System (LASS), Quantimet Q570 Image Analysis System, Quantimet Q600 image analyser, 3D laser-digitising system and Council for Scientific and Industrial Research (CSIR). The image analysis methods that do not belong to the Photograph analysis or the image analysis systems are classified as "others" in Table 6. In the Table 3-7, the applied apparatuses, image acquisition (raw data), the study highlights and the output (morphology indices) are introduced.

2.1.1.1.1 Apparatus and raw data

The applied apparatuses in SIA methods include the camera, X-ray CT scanner, laser scanner and 3D scanner. The camera takes the digital 2D particle image and is mainly utilised in the Photography analysis (PA) methods. The X-ray CT scanner obtains the cross section image of the particle, and the cross sections of one particle can be reconstructed to make one 3D particle image. The laser scanner sheds the laser beams onto the particle surfaces, after using the black and white camera for photographing the image of the scene, the uneven surface is indicated by appearing the reflected laser beams as a dashed line. The 3D scanner takes the particle images from various viewpoints and recombine the images to form the 3D particle image, as shown in Figure 2 (described in detail in [57]).

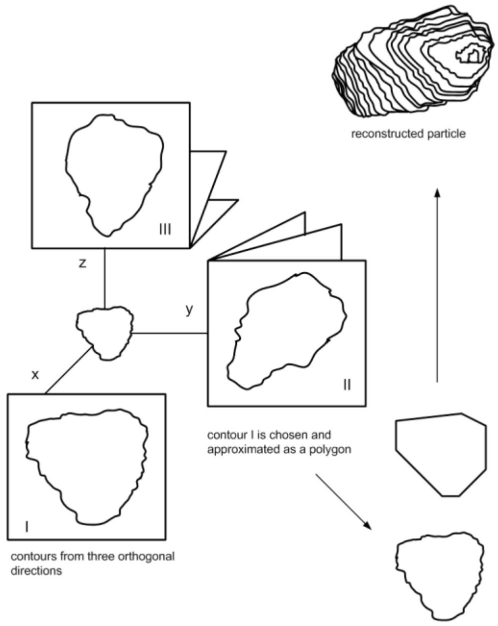

Figure 2 Principle of imaging from multiple views (reproduced from [58])

In the various SIA methods, the above four kinds of apparatuses are utilised dissimilarly for better image acquisition. For example, in [59], with the laser scanner the whole particle is scanned, whereas the LASS system only scans the upper sides of particles [60]. Another example of prominent difference is taking the particle images from various view sides, comparing with some methods that only take one particle image, as shown in the Table 3-7. Also for better image acquisition, in the image analysis systems, the apparatuses are combined with some other facilities (e.g. transparent trays [60], green backlight [61]). each apparatus has the advantages and the disadvantages, as shown in Table 1.

Table 1 Advantages and disadvantages of the apparatuses

Analysis method	Advantage	Disadvantage
Photograph analysis	Cheap; easy to access	Human intervention to appropriately arrange the particles
AIMS; AIMS2	Measure three particle axes; capture particle images at different resolutions based on particle size; measure particle surface texture.	Good contrast requirement between particles and background; expensive
UIAIA; E-UIAIA	Use three cameras to capture three images of one particle moving on a conveyor belt; measure particle surface texture	Uses same camera magnification to take images of all particle sizes
LASS	Measures the three dimensions of aggregates; half 3D particle image; scan several particles each time	Use the same scan to analyse different size particles; considerable manual work
3D laser-digitising system	Complete particle information	Low efficiency; considerable manual work
X-ray CT scanner	Complete particle information	Low efficiency; time-consuming reconstruction for 3D image;

By different apparatus utilisation way, the obtained raw data types are different. In the PA methods, they include unique image of particle, unique image of particles, two/three images of particle and two images of particles. In the analysis systems (Table 5) and other methods (Table 6), the raw data have more types, i.e. One grey image and one black and white image, three orthogonal images of particle, upper side of particle and 3D image.

The unique image of particle is taking only one image for one particle, and the unique image of particles means to take one image for several particles, which is for saving time but requiring more complex algorithm (image segmentation). For higher accuracy of image analysis results, two or three images of one particle from different view sides are applied, resulting to the raw data types of two/three images of particle. For the other types, in the AIMS, different shape scales are analysed with different images, specifically, the one grey image is for surface texture and one black and white image is for form and angularity. Three orthogonal images of particle are taking the images of one particle from three orthogonal directions (UIAIA). The LASS utilises the upper side of particle as raw data type, which is the half of one particle, whereas some types utilise the complete 3D image for one particle.

The analysis result accuracy is significantly influenced by the raw data types. Initially, unique image for one particle is utilised for image analysis, and improving the image resolution is the only means for higher accuracy analysis (e.g. [62, 63]). The resolution of the digital images has effects on the image analysis results, because higher resolution can present clearer particle outline with more pixels, which can reduce the calculation error of the perimeter and area of the particle, especially for the surface texture evaluation. However, two limitations need improvements. One is the low efficiency of photographing particle one by one in a sample. The other is that a single 2D image for each particle causes the inaccuracy of measuring the particle information (e.g. volume and thickness), which are mostly inferred from a 2D particle projection.

To overcome the low efficiency limitation, the whole sample is placed in a proper position and photographed [61, 64-68], and many particle image segmentation algorithms are proposed for precise and automatic extraction, especially with the cutting-edge computer technology. For example, based on the convolutional neural networks (CNN), Tong presents an efficient and automatic PA method to evaluate particle angularity through digital images [69]. It is proved that the CNN can locate and abstract each particle from a digital image of particle assemblies by dividing it into several overlapping sub-windows for extracting image features.

Towards the second limitation, many solutions are proposed using more advanced apparatuses or other aided facilities. For example, the transparent plastic trays are used with two perpendicular faces for attaching the particles and then photographing other particle sides automatically [70]. This can be more efficient than the earlier methods, i.e. the human intervention for proper particle arrangement (e.g. [71, 72]). In [73], with a special cylindrical carrier, the image of particle shadows can be utilised for the measurement of three axes. A camera and two lighting sources are utilised for obtaining the image of the perpendicular particle shadows, which are processed to measure the three principal particle axes. Even though the two methods can measure three particle axes, there still exists plenty of inevitable manual work. The work is replacing the particles on the plexiglass holders or the cylindrical carrier with new particles.

In addition, in the image analysis systems, the aided facilities can help to obtain more particle information, leading to more efficient and accurate morphology evaluation. For instance, the UIAIA/E-UIAIA places particles on a conveyor belt and employs three cameras for three orthogonal particle images, as they consider that two images lost vital particle information, causing imprecise morphology evaluation. The AIMS/AIMS2 utilises two cameras to take one black and white image and one grey image for particle outline and surface texture respectively, and the particle thickness can also be estimated when taking the particle outline. Although both systems successfully obtain the 3D particle information, it still needs to arrange the particles in proper positions, so that two or three images of one particle can be captured simultaneously. More importantly, in all the above-mentioned methods, despite using three camera views, inferences must be performed based on 2D projections for particle 3D characteristic evaluation.

More advanced apparatuses include the 3D scanner, laser scanner and X-ray CT scanner, and can help to obtain complete particle information (e.g. volume, surface area) through 3D image or half 3D image. In the LASS, the half 3D image is utilised for shortening the scanning time, however, the three axes cannot be precisely computed. Complete 3D image can provide the complete particle information, however, performing all the above-mentioned apparatuses and processing the image are time-consuming (e.g. merging two half 3D images [59]). For example, as reported in [59], X-ray CT scanning takes about 20 min to complete one particle scanning operation, and the post-processing of the scanned data costs even more time. That is due to the scanning equipment efficiency and the post-processing software. The scanned data should be processed and analysed with external software. This is also commonly found when utilising the other advanced apparatuses, i.e. the 3D scanner and the laser scanner.

From the discussion of the apparatuses and raw data types, the advantages and disadvantages can be seen, furthermore, the development trend can be observed as well. Specifically, the raw data types are the only one 2D image for one particle, afterwards, two/three 2D images for one particle or particles emerge. Finally, the complete

3D image is utilised for particle morphology evaluation. Moreover, more and more advanced apparatuses are utilised for image acquisition with higher and higher resolution. However, the main problem is the efficiency when not only applying the advanced apparatus but also using the cameras with aided facilities.

2.1.1.1.2 Study highlights

In the Table 3-7, the study highlights describe the main results or progress that are achieved in the literature, including raw data process and morphology-related performance.

Raw data process

The raw data process is the means to process the image for conveniently obtaining the particle information. For example, the binary images are obtained after a kind of 2D digital image process for better performing other image process procedures (e.g. Dilate, Open, Close-, Fill Holes, Watershed, etc. [74]). Another example is the 3D image process in [20, 46, 59, 75], which is combining the two half 3D images of one particle into the complete 3D image. Likewise, the 2D radiographies of one particle (from X-ray CT scanning) can be reconstructed into the compete 3D particle image [45, 76]. The raw data process is mainly performed with some commercial software or programming codes. More information can be found in the Table 3-7. It needs to note that the Fourier series utilised for morphology evaluation is emphasized in the study highlights as an important raw data process means and discussed particularly in this sub-section.

Morphology-related performance

The morphology-related performance is also described at the study highlights in the Table 3-7. Currently, limited studies were performed on the particle morphology on the ballast performance, for this, they are emphasized as a promising research prospective. For example, in [54], the base course performance is related with the particle morphology (form, angularity and surface texture). Another example in [77] proves the strong correlation between particle morphology with the drained friction angle and void ratio. The effects of particle morphology on ballast shear strength is studied in [78], demonstrating the correlation also exists in the ballast particles. Even though some related studies have performed, it is still not sufficient to draw a recognized conclusion. This is due to limited studies were performed, and more importantly in the studies only 2D image/images for one particle were utilised other than 3D images. Additionally, the ballast degradation was not considered during the studies.

The Fourier series is the definition of an image process means for image analysis using the Fourier transform. It can be used for image analysis to quantify the form, angularity, and surface texture of the particle. This method has been developing from analysing 2D images to 3D ones over years. Subsequently, the calculation methods for image process have been advancing as well.

Fourier series

In the Table 3-7, how the Fourier series is utilised is described in details. Specifically, unrolling the particle outline into polar coordinates or rectangular coordinates is the first step [63, 65]. Afterwards, comparing the shape descriptor values of regular shapes (e.g. triangle, rectangle) with those of particles can quantify the particle shape [65, 79]. Using the cumulative error (amplitude of the radial vector) or area ratio between the reconstructed particle profile and the original one, the particle shape can be quantified as well [80, 81]. All the above-described Fourier series means are based on the 2D image. In [82], the 3D image is processed with the Fourier series, however, only the particle reconstruction is achieved with this. It needs to note that in the LASS, the Wavelet transform is a Fourier series means for 3D image. It is decomposing a signal (polar coordinates of particle upper surface) into a group of linear combinations. Afterwards the mother wavelet is dilated and translated. The morphological indices are calculated by determining how well the dilated and translated versions of the mother wavelet coincides with the signal [51]. The fine scale wavelets represent surface texture (also used by AIMS), while the larger scale wavelets characterise the form or angularity. That depends on the enlargement degree of the mother wavelet.

The advantages of the Fourier series methods can be summarised. On one hand, some of the Fourier series methods are utilised to analyse 3D particle images for more accurate particle shape evaluation. The methods started from analysing 2D images, afterwards the 3D images can be analysed with the Spherical harmonics series or Wavelet transform. According to the authors' knowledge, to date only using the Fourier series methods can calculate morphological indices for the angularity of 3D particle images. On the other hand, the Fourier series provides different shape quantification methods from the methods used in earlier studies. To be more specific, the three particle shape characteristics (form, angularity, and surface texture) can all be quantified by the same function (e.g. Wavelet transform), while most of the other methods quantify the particle shape with particle geometrical properties (e.g. area, perimeter, volume and three particle dimensions).

2.1.1.1.3 Outputs

In the Table 3-7, the output contains the form, angularity, surface texture, size and degradation. The definitions of form, angularity, surface texture and size have been introduced at the beginning of Section 2.1.1 (Shape and size evaluation). The degradation evaluation is also introduced as a kind of output based on the image analysis results. Specifically, the degradation is mostly quantified by comparing the morphological indices change before and after tests or the in-site tests/operations.

Form

Using the geometrical characteristics (obtained with image analysis), the morphological indices for particle form can be calculated. For the 2D images, the geometrical characteristics include perimeter, area, Feret dimeter, three particle axes, inscribed circle, circumscribed circle and equivalent ellipse. For the 3D images, the geometrical characteristics include volume, surface area, three particle axes, equivalent ellipsoid, equivalent sphere, circumscribed sphere. The morphological indices calculated with the characteristics are given in the Table 3-7, and the calculation methods are described in the Table 8-12 (with hyperlinks).

The Sphericity (Circularity for 2D analysis) or Flat or elongated ratio are the most widely-used indices, and various calculation methods for this index can be found in the literatures. For example, one kind of calculation methods utilises the ratio of particle volume to circumscribed sphere volume or the ratio of particle surface to that of equivalent sphere. Other calculation methods are mostly based on the three particle axes. However, the Sphericity [15] illustrates a surprisingly high association with Krumbein's Roundness [48], notwithstanding Sphericity and Roundness are regarded as the morphological indices for form and angularity, respectively.

Therefore, some morphological indices are proposed to present the particle form differently, e.g., the modified true sphericity [59] and Ellipsoidness [50] (Ellipseness for 2D [83]). They are expressed by combining the equivalent ellipsoid (equivalent ellipse for 2D) and three particle axes. These morphological indices show little correlation with Roundness or particle size. Other than modifying the Sphericity, the Form index is proposed using different calculation methods. To be more specific, one calculation method utilises the deviation of the global particle outline from a circle [77]. The other one is in the AIMS/AIMS2, which calculates the incremental changes in the particle radius in all directions [84]. However, whether the indices present the form precisely is not clear and no studies have been found to compare these indices to check the feasibility and differences. The same question can be found in the angularity or surface texture evaluation.

Angularity

The morphological indices for particle angularity contain the Roundness and Angularity index. The Roundness (common in earlier studies) is computed with the geometrical characteristics, i.e., three particle axes, perimeters/radii of corners (or convex parts), particle outline area and particle outline perimeter. For instance, in [15], the Roundness is expressed as the ratio of the radius summation of corners to the inscribed circle. Afterwards, in the later studies, the Angularity index is proposed and computed by measuring the corners' angles instead of their perimeters/radii. An example can be found in [85], which utilises the corner angles, the distance of the corner tip to the centre and the inscribed circle radius. The latest Angularity index calculation method is proposed in the AIMS/AIMS2, which is applying the Erosion-Dilation technique. It calculates the area change ratio after the Erosion-Dilation operations. Another cutting-edge calculation method is based on the probability of the adjacent subtended angle change (UIAIA/E-UIAIA).

However, these calculation methods are based on the 2D images, which is not accurate especially applied for railway ballast. Because ballast particle size is larger, compared with the sands or soils. The different view of the particle will provide the different results. This problem is more severe when calculating morphological indices for particle surface texture.

Surface texture

Specifically, most of the calculation methods are based on the 2D particle outline (examples in [54, 56, 66]). In [54], the method computes the ratio of the particle outline perimeter to the convex perimeter for evaluating surface texture as the Roughness (morphological index). This is not accurate, because the particle can be considered as the combination of large amounts of the particle outlines. Towards this issue, the Wavelet transform is proposed to analyse the surface texture from the grey particle image (LASS/AIMS/AIMS2), which is more accurately than only analysing one particle outline. The Wavelet transform is an image process means using the Fourier series. Based on that, the Surface texture index is proposed in the later studies [51, 86]. It needs to note that most of the morphological indices for particle surface texture apply the Fourier series, e.g. [65, 79-81].

Size

Particle size is based on one of the three particle axes, volume or area. For instance, the AIMS or AIMS2 evaluates the form with the Flat or Elongated ratio. During this evaluation, the three dimensions of a particle are measured and one of them can be used as the particle size. Another example to measure the particle size utilises the equivalent diameter (based on the particle surface area) [87]. Instead of measuring the sizes of particles one by one, more efficient methods for measuring the particle sizes are proposed. The method is taking a photo of the entire particle sample, and then drawing the particle size distribution of the sample [61].

Volume is evaluated with the images from the three orthogonal views, as proposed in the UIAIA/E-UIAIA with the average absolute error is at 11.5% [42]. The LASS utilises the upside 3D image for volume calculation, but it needs modification [88]. With higher accuracy, another two methods are proposed, utilising the 3D X-ray images to calculate the particle volume and surface area. Higher accuracy measurement of the volume and surface area of particles can contribute to better size measurement and shape evaluation. To measure them more precisely, the cutting-edge technical devices are used for more high-resolution images. Also, the images are developing from 2D to 3D until the error of the volume measurement is less than 0.1% [20]. However, obtaining the 3D particle image costs large amounts of time. From the discussion, it can be seen that the image analysis methods can be utilised to obtain particle size distribution. They are more accurate than traditional sieving.

Almost all the methods with 2D images are still analysing the binary image or projection of particles. That means the geometrical properties (for morphological index calculation) are still measured using the particle outline. This will significantly influence the accuracy of the particle shape evaluation because of two aspects. On one hand, the particle outline can only provide two dimensions (i.e. the longest and shortest axe). When the particle image is taken at another side, the results of the dimensions will be quite different. On the other hand, the surface texture cannot be fully quantified. The roughness of the particle outline was utilised for the particle surface texture in [54, 66, 89], their details are given in Table 10 (Hyslip & Vallejo, 1997; Janoo, 1998; Kuo et. al., 1998). However, one particle outline roughness cannot reflect the surface texture of the whole particle, unless using more outlines of the particle. As reported in [81], when the number of the particle outlines are more than 30, the average quantification value of the surface texture becomes stable.

Degradation

Most particle degradation evaluation methods using image analysis are based on the particle morphology change. They compare the differences of morphological indices after laboratory tests. For generating deteriorated particles rapidly, the laboratory tests are performed, i.e. Los Angeles Abrasion (LAA) test or the micro-Deval test. The description of the two tests can be found in [37]. The laboratory tests are utilised for deteriorating ballast particles, because that has the advantage of controlling the degradation stages (or degree) by setting the testing duration. Two types of testing duration can be set. One is by setting the revolution number of the LAA tests (or micro-Deval tests), e.g. [45, 61, 90, 91]. the other is by setting various testing time, e.g. [92, 93].

Besides the laboratory tests, the image analysis is also utilised for the ballast degradation study in the field [94]. The image analysis method is an automated alternative, machine-vision-based inspection system. It has the potential to directly and objectively evaluate the condition of ballast layer and degradation levels with ballast layer image, which are captured in the field. More importantly, the imaging-based index, average Percent Degraded Segments (PDS) was proposed and successfully implemented for evaluating different levels of ballast degradation with the images of ballast layers.

In most studies, the degradation is evaluated by the particle size change, presented by the shift of the PSD, e.g. [61, 91, 95]. However, during the degradation, the particle abrasion/breakage cannot be precisely evaluated or reflected only with the PSD change. Therefore, the shape change is presented by the distribution shift of the Flat or elongated ratio (for form) in [61, 95]. After development, more specific morphological indices (for form, angularity) applied in degradation study can be found in [92]. In this study, the distribution of the two morphological indices are presented, i.e. Aspect ratio and Angularity index. However, this study did not evaluate the surface texture reduction. In the studies [91, 93], the surface texture reduction is presented by the distribution change of morphological index for surface texture (Surface texture index).

However, the methods for degradation evaluation are generally performed on a 2D basis. This means the measurement of the particle morphology, especially the angularity, are mainly dependent on the orientation and posture of the particles. Consequently, it is necessary to perform the degradation analysis and develop degradation evaluation methods based on 3D images. For example, in [20], the two 3D images of one particle are compared (before and after LAA test), and the results show that the main degradation mechanism is the sharp corner loss (angularity reduction). In this study, the single particle degradation is presented instead of the earlier studies that evaluate the morphological indices' change of a whole sample. In addition, the results of degradation evaluation are visible and reliable, demonstrating the feasibility of developing 3D degradation evaluation. However, this method still needs further modification, such as, to shorten the scanning duration time.

Among the earlier studies, 3D image analysis is the most potential and effective for degradation evaluation, nevertheless, it still needs more development and further studies. Because most of the methods (2D or 3D) were estimating the abrasion degree, and few evaluation methods were established for the other degradation type, e.g. particle breakage. Furthermore, the only study, proposing image-based particle breakage evaluation method uses the 2D image to obtain the change of the PSD [96], and accurate particle breakage evaluation is difficult to be performed. Consequently, more studies on 3D image analysis should be performed for a deeper understanding of the ballast degradation mechanism and its effect factors. More importantly, understanding those also help further studies on ballast performance and deformation considering the ballast degradation.

2.1.1.2 Dynamic Image Analysis

In this sub-section, the DIA methods are introduced, and they are classified in the following aspects. The classification is according to the apparatus. The specific of these methods are given in the Table 7, including, the apparatus, raw data type, study highlights and output.

- the Micrometrics OptiSizer System,
- the Video Imaging System,
- the Buffalo Wire Works System,
- the VDG-40 Videograder,
- the Computer Particle Analyser,
- and the Camsizer.

2.1.1.2.1 Apparatus and raw data

The above-mentioned DIA methods rapidly obtain the particle images, avoiding a lot of manual work. The methods provide a rapid alternative means for capturing and processing 2D digital images to present the PSD. Mostly, the CCD camera (i.e. line-scan or matrix) is utilised for rapid image acquisition. The matrix CCD camera captures 2D image in each photographing, whereas the line scan camera captures narrow stripes of particle that are subsequently reconstructed into a 2D image. The line-scan CCD camera captures a more accurate falling particle image, due to it scans every strip sequentially. However, with the matrix CCD camera, the odd lines (or every other line) are scanned in the first pass and the even lines are scanned during the second pass. Therefore, the matrix CD camera method is adequate for SIA methods, but it will produce error when photographing falling particles.

The raw data types were introduced in the Sub-section 2.1.1.1.1, and they are also applicable for the DIA methods. the raw data types of the DIA methods are given in Table 7. Whereas, the advantages, disadvantages and some other information of these methods are given in Table 2.

Table 2 Comparison of the DIA methods [97, 98]

Name	Camera	Scanned sample type	Advantage	Disadvantage
Micrometrics OptiSizer System	Matrix CCD camera	Portion of particles	Measure large particle form	Cannot measure angularity or surface texture; assume particle as idealized ellipsoid; use one camera magnification to capture different sizes' particle images; Separate vibratory feed systems; backlights required for both fine or coarse particles
Video Imaging System	Matrix CCD camera	Portion of particles	Measure large particle form	Cannot measure angularity or surface texture; assume particle as idealized ellipsoid; use one camera magnification to capture different sizes' particle images; Separate vibratory feed systems; backlights required for both fine or coarse particles

Buffalo Wire Works System	Matrix CCD camera	Portion of particles	Measure particle form	Cannot measure angularity or surface texture; 2D form index
VDG40 Videograder	Line-scan CCD camera	All particles	Measure large particle form, especially, the Flat or elongated ratio	Cannot measure angularity or surface texture; assume particle as idealized ellipsoid; use one camera magnification to capture different sizes' particle images
Computer Particle Analyser	Line-scan CCD camera	All particles	Measure large particle form	Cannot measure angularity or surface texture; assume particle as idealized ellipsoid; use one camera magnification to capture different sizes' particle images
Camsizer	Two matrix CCD cameras	All particles	Measure particle form and angularity; two cameras to capture particle images at various magnifications based on particle sizes	Cannot measure surface texture; assume particle as idealized ellipsoid

2.1.1.2.2 Study highlights

Raw data process

The 2D images of falling particles are processed with various kinds of image transformation algorithms respectively. Raw data process of these DIA methods is performed by various kind of proprietary software, which are developed by the device developers or companies. In these kinds of software, the process involves various assumptions to provide a 3D particle form evaluation. For example, in the Micrometrics OptiSizer System, the spherical type analysis converts each imaged particle profile area into a circle with equal area. The volumetric information is calculated with the radius of the circle as a sphere volume.

The DIA methods can accurately and rapidly measure the size and the two dimensions of particles. However, their limitation is that they cannot sufficiently evaluate the particle angularity or surface texture [99]. That is due to the lack of enough development in the image processing methods and the morphological indices have not been utilised in these methods. Moreover, the CCD camera might not be fast enough to photograph the falling particles. Additionally, when particles are falling, they might change orientation or rotate, which could cause inaccuracies. Most importantly, there are the potential that particles are overlapped during falling.

2.2 Discussion

In this section, the image analysis methods for particle morphology evaluation are summarised. They include the manual methods and methods using image analysis. The image analysis methods are categorized as the Static Image Analysis (SIA) and the Dynamic Image Analysis (DIA), and the apparatuse raw data type, study highlight and the output were introduced. Giving the pros and cons of the image analysis methods can help researchers easily compare calculation methods and find the proper method that is suitable for their research. More importantly, analysing the limitations will assist to find insufficient points that can be improved. After introducing the image analysis methods, the areas for improvement can be observed for better morphology evaluation, such as, from 2D image analysis to 3D image analysis, a comprehensive morphological index, and a both efficient and accurate image analysis method, etc. They are discussed later in the Sub-section 4.1.

Better morphology evaluation can assist to study the effects of the ballast particle morphology on the performance and deformation more accurately and convincible, as discussed in the Sub-section 1.1. However, until now, according to the authors' knowledge, only one study has been reported with image analysis methods to study the effects of ballast particle morphology on the performance and deformation [78].

Using the 3D image and corresponding image analysis methods, the geometrical properties can be measured with high precision, e.g. the volume, surface area and three dimensions of the particle. Almost all the corresponding morphological indices utilise these geometrical properties to quantify the form and the angularity of the particle. It is undeniable that precisely measuring the geometrical properties can help improve the accuracy of the particle shape quantification. Moreover, the precision can still improve with the development of the image acquisition and processing means.

However, most of the morphological indices are still calculated based on the volume, surface area and three dimensions of the particle. More advanced calculation methods should be developed based on the precise data of 3D particle image. For example, the three dimensions of the particle are still utilised for the form quantification [46], even though the distance between any two points on the particle surface can be measured with the 3D particle image. This is not utilised in any reported studies. More importantly, few studies are devoting to the angularity and surface texture quantification with 3D images. It should be noted that the Fourier series is the only method that the authors can find until now to analyse the 3D angularity.

3 Rheology

The particle rheology mechanism is characterised by translation and rotation of individual particles. According to the studies so far, it has been demonstrated that ballast performance and deformation of ballast bed are mostly dependent on the ballast particle rheology. The irregular geometry of ballast track, such as the hanging sleeper due to the differential settlement, is usually caused by large ballast particle rheology. Consequently, the potential damages to the sleepers, fastening system and rails would emerge, hence, it is significant to study the ballast particle rheology.

However, the research on ballast particle rheology are mostly performed with numerical simulations, and a limited number of studies were by tests with sensors or transducers. Numerical simulations could only reflect the quasi-static ballast particle rheology, while the tests can only present the particle rheology of some limited positions, where the sensors or transducers are placed.

Therefore, the image analysis methods for the rheology study on granular materials will be reviewed and discussed in this section, providing a deep exploration of utilising the image analysis for ballast particle rheology study. Particularly, the Particle Image Velocimetry (PIV), as a technique for analysing digital images, can measure the particle displacement and velocity etc., and its application for granular materials (sands and soil) will be introduced in this section. Finally, some image analysis methods for ballast particle rheology study are presented in the last sub-section.

3.1 Particle Image Velocimetry

With the rapid development in digital imaging acquisition and processing technology, image analysis is feasible to measure the displacement/strain of the granular materials. As a member of image analysis techniques, the PIV was first proposed to measure the velocity of the gas or fluid. It measures the motion of the target markers in a fluid, and observes the locations of the target markers at two or more time points [100]. Its fundamental principle for the velocity measurement is the evaluation of the local velocity $\boldsymbol{u}$ from

Equation 1 $$u(x,t) \doteq \frac{\Delta x(x,t)}{\Delta t}$$

where, $\Delta \boldsymbol{x}$ is the displacement of a target marker, located at the position $\boldsymbol{x}$ at the time $\boldsymbol{t}$, while $\Delta \boldsymbol{t}$ is the short time interval between two observations.

The rheology of soil particles could be treated as a low-velocity flow process, and hence the PIV (after improved) was firstly applied for the non-contact measurement of soil deformation in geotechnical tests [101]. Its main improvement is the detection of the soil displacements without installing target markers. Because when using target markers, the number of measured targets is limited, which could not reflect the rheology of the whole sample.

However, there still exist some difficulties when applying the PIV in geotechnical tests. For example, the success of the test depends on the variation of intensity or texture in the images, however, it was found necessary to enhance the texture by adding reflective particles. Despite this difficulty, it is convinced that the PIV would ultimately be applied to similar geotechnical studies, owing to the fast development of image processing technology, as well as better image texture with higher-resolution cameras [102]. Another difficulty in PIV is the determination of the correlation between the image and object coordinates. To solve that, more complex procedures for camera calibration using the three-layer back-propagation neural networks algorithm, was proposed. The algorithm helps to provide more accurate results, which are independent of the angle between the image plane and the object plane, and its rapid and accurate calibration will extremely facilitate the PIV application into geotechnical tests [103].

The rheology of sand particles can also be treated as a low-velocity flow process, and therefore, it can be also studied with the PIV. For instance, the rheology of sand particles around the rigid ribbed plate was studied with a direct shear box plus image analysis. The direct shear box is built with plexiglas walls in order that the CCD camera can observe and measure sand particle displacements. Using the devices, the main work includes monitoring the individual sand particle movements, mapping the dilation and contraction zones, as well as showing the shear strain [104].

Another example is that series of biaxial tests on sands are performed with a CCD camera recording the specimen deformation during compression. A square grid pattern is printed on the latex membrane surface, and the deformation is detected by noting the grid displacement. Based on the comparison of selected images (captured from the video), the shear band formation analyses are performed to characterise the specimen failure and to compare with two other classical methods [105].

Without printed grid pattern on the latex membrane surface, the biaxial tests are performed on dense sands. The image analysis was used to show localized displacements, to quantify the shear band volumetric strains, and to measure the shear band inclination and thickness. The displacements are measured with higher accuracy by matching pixels between the digital images, and can be further used for the volume strain calculation. The shear band inclination and thickness can be computed because the shear band boundary can be clearly defined from the images [106].

Boldyrev demonstrated that the PIV can be used to study not only the sand rheology, but also the rheology-related performance or deformation [107]. The PIV can obtain the following parameters: particle displacement vectors, particle vertical and lateral displacements, shear and volume strain. It was applied for the two following tests. One is load tests in a chamber with one plexiglas wall, specifically, two sand specimens (with or without geogrid) are loaded respectively with a test plate in plain strain [107]. The other test on sands is performed in the same chamber but with the specimens penetrated by a pile. It examines the sand deformation pattern during the continuous penetration with the PIV to measure the strains, including the shear strain, dilatational strain and the depth and width strain development [108]. It is concluded that the PIV can evaluate sand rheology and the rheology-related performance or deformation both quantitatively and qualitatively.

Besides the measurement of the particle displacement or velocity, the PIV can also quantify the particle rotation when applying 2D assembly of disks as ideal particles [109]. Therefore, for achieving that, two or more identifiable points need to be followed for each disk. Specifically, the orientation θ of each disk can be defined based on the centroids of the two identifiable points, **(x_c, y_c)** and **(x_s, y_s)**:

Equation 2
$$\theta = \arctan\left(\frac{y_s - y_c}{x_s - x_c}\right) \qquad \left(0 \le \theta < 2\pi\right)$$

Equation 3
$$\Delta\theta = \theta_j - \theta_i \text{ (counterclockwise positive)}$$

It needs to be noted that the two identifiable points are the centroids of the central and side markers on one disk respectively.

From the introduced studies, it can be concluded that the image analysis can be utilised for the rheology study on granular materials, such as soil and sands. Particularly, the PIV (image analysis method) is efficient and accurate for the rheology and rheology-related study for the performance or deformation. Accordingly, it can provide a potential utilisation for railway ballast rheology study, which is relatively unexplored until now. Therefore, the existing applications of image analysis for ballast rheology study are introduced and discussed in the following sub-section. Whilst, some PIV applications for ballast rheology study are also introduced for its future promising utilisation in ballast particle rheology study.

3.2 PIV for railway ballast

Until now, the study on railway ballast rheology is at the initial stage, and it should be focused because the ballast performance and deformation are mainly dependent on its rheology. Some studies have been performed on ballast rheology, however, they could reflect the rheology only at a limited degree. Using the image analysis can efficiently and accurately track all the particles' trajectory during motion, thus it can deepen the understanding of the effect of particle rheology on the performance and deformation.

For instance, with the lateral view of the whole sample captured periodically by a digital camera, a sinusoidal loading is performed on assemblies of prismatic mineral particles, as shown in Figure 3 (an early-stage PIV example). This article mainly uses the results for the validation of the discrete element simulation in the LMGC90 platform, including the settlement and the displacements [23]. The displacement and settlement results demonstrate that the photogrammetry technique can become a tool for ballast rheology study and can be developed further, even though the ballast particles in this test are simplified and scaled down as prismatic particles. The simplification is performed only for matching the element shape in the LMGC90 program.

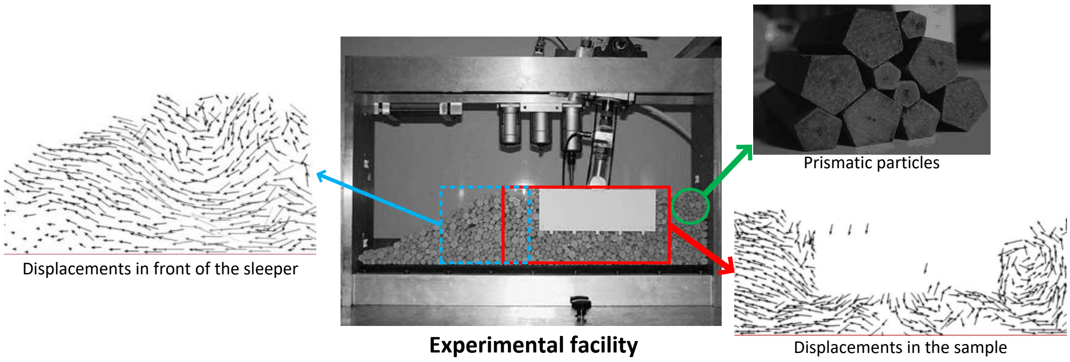

Figure 3 Experimental facility and the displacement results (Modified after [23])

With the development of digital image processing and analysis, the PIV becomes more powerful with more applications in the ballast rheology study (or rheology-related study). For example, the volumetric strain during the triaxial tests can be computed with the PIV by tracking and measuring the movement of the patches painted on the triaxial specimen (Figure 4a). The obtained radial volumetric strain results (different elevations on the sample) is compared with the results (measured by wire extensionometers), demonstrating the possibility and efficiency of the PIV for volumetric strain measurement [110]. However, strain measurement with the PIV is still not sufficient for the ballast rheology study (or rheology-related study), because the translation and rotation of ballast particles cannot be reflected directly from the radial volumetric strain change.

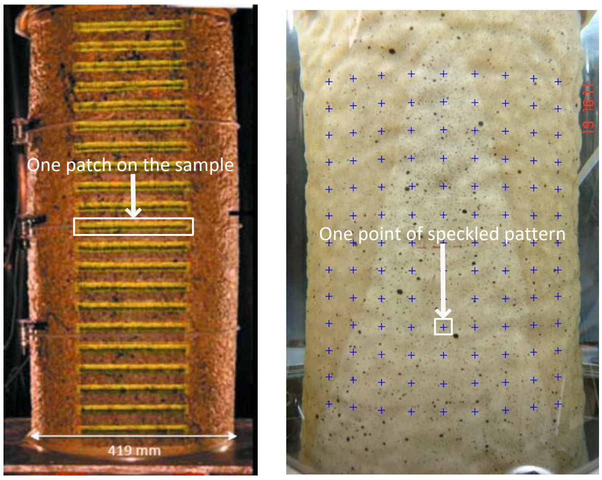

a b

Figure 4 Markers on triaxial specimen (modified after [110] and [111])

Towards these issues, a modified PIV method (proposed in [112]) is utilised for the deformation measurement (principal and maximum shear strains) in the triaxial tests of 1/3rd and 1/5th scaled railway ballast (Figure 4b). From the figure, the markers for tracking have been improved into a speckled pattern, and it can measure the displacements in both the x (circumferential) and y (vertical) directions [111]. The improved PIV method could partly solve the issues by tracking more monitoring points, which can reflect the deformation more accurately and efficiently. However, it still needs improvement when applied for the ballast rheology study (or rheology-related study), because the deformation is measured based on the displacements of the monitoring points rather than the particles.

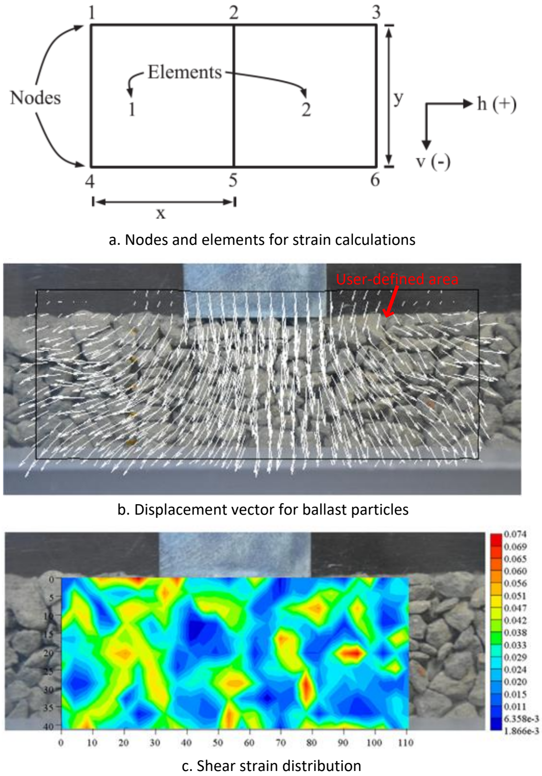

Figure 5 Strain calculation method and distribution (modified after [74])

Without markers, the deformation and the strains for elements/meshes (Figure 5) could be calculated according to the displacements of node points (like the markers). The calculation method for strains is shown below. For example, the vertical strain at element 1 (Figure 5a) could be obtained with the strains between nodes 1 and 4 ($\varepsilon_{v,1-4}$) and between nodes 2 and 5 ($\varepsilon_{v,2-5}$), as given in Equation 4.

Equation 4 $$\varepsilon_{v,1} = \frac{\varepsilon_{v,1-4} + \varepsilon_{v,2-5}}{2}$$

Using the strains of all the elements, the strain distribution could be obtained, as shown in Figure 5c. The improvement is that the number of node points can be determined automatically by users instead of manually-painting markers, which is achieved by tracking the motions of the same or similar pixels on a user-defined area in an image (Figure 5b). However, the displacements obtained by tracking the node points are still not the particle displacements, although the point number can be large enough in high-resolution images [74, 113]. The introduced examples demonstrate that using the PIV for rheology study of every ballast particles has not been studied so far.

Nevertheless, the PIV is developing step by step, and it is used in more tests, providing more reliable results. For example, in the rheology study of ballast bed under cyclic longitudinal loadings [114], the PIV is used for tracking the motion of ballast particles, as well as revealing the ballast deformation mechanism and the longitudinal resistance performance. Additionally, this method is worth modification and can provide a potential solution to the difficulty of displacement and velocity tracking of every particles. For instance, tracking the rotation of the ballast particles has not been explored, while in the introduced study [109], this has been successfully applied.

4 Discussion and perspective

This paper reviews the studies on using image analysis to study the morphology, rheology and degradation of granular materials (soil, sands and ballast etc.), due to their significant effects on the ballast performance and deformation. The main aim of this review is to gain insights into the application of image analysis for ballast studies, including the morphology, rheology and degradation.

Regarding the morphology, the image analysis methods are introduced, as well as their utilised morphological indices. Moreover, the correlations between the morphological indices and performance or deformation are also presented. Concerning the rheology, the PIV is introduced as a promising image analysis method, for analysing the rheology and rheology-related performance or deformation of granular material layer. Finally, the image analysis methods for particle degradation evaluation are introduced.

From the presented image analysis methods, it can be concluded that there still exists some research gaps and aspects for improvement. They are proposed and discussed in the following three sub-sections.

4.1 Morphology

Concerning the morphology, most of the studies focused on using image analysis to replace the traditional measurement methods for accurate particle morphology quantification. In most cases, the shape is categorised into three aspects, the form, angularity and surface texture. Moreover, the size could be evaluated using the morphological indices for the form. The reviewed studies demonstrate the feasibility of image analysis for particle morphology quantification with higher accuracy. However, the image analysis methods may still need improvement at the following aspects.

From 2D to 3D

The development tendency of image analysis is from 2D to 3D. The image analysis started from the 2D projection or binary image analysis, afterwards, images were taken at two orthogonal directions for higher accuracy. It should be noted that the binary image is similar with the projection. To meet the requirement of higher accuracy, two solutions were proposed. One was utilising the laser scanning to obtain one side image of the particle. The other one was to acquire images at three orthogonal directions. However, they are still not sufficient to present the real particle morphology, because the projections or binary images could not provide the accurate morphological indices until the number of binary images or projections is large enough.

After the emergence of 3D image acquisition technology, such as the 3D X-ray, laser scanning etc., several studies were performed with them. From the studies, it was demonstrated that the 3D image analysis methods can present the real particle morphology. More importantly, 3D image analysis is more promising at high accuracy and resolution for even tiny surface details, and it does not enlarge the particle morphology. Furthermore, 3D image analysis enables the quantification of the particle edge, 3D angularity and 3D surface texture, which are still relatively unexplored.

Comprehensive morphological index

It is more convenient and efficient to combine the three shape characteristics (form, angularity and surface texture) and develop one comprehensive morphological index. Most of the studies estimated the shape characteristics, the form, the angularity and the surface texture respectively, and correlated them respectively with the performance or deformation. However, all of them contribute to the performance and deformation, in other words, it is not accurate to correlate one shape characteristic with the performance or deformation when ignoring the other two. Consequently, it is necessary to create a comprehensive morphological index using the combination of the three or more characteristics e.g. the particle edge.

Efficient and accurate analysis

It is necessary to improve the image processing and analysis efficiency. Current measurement methods based on image analysis are either accurate but not efficient or fast but not accurate. For example, the Dynamic Image Analysis method, the VDG-40 Videograder (introduced in Sub-section 2.1.1.2) is fast to obtain the particle morphology, however, the obtained form or angularity are not as accurate as the results from 3D image analysis. Whereas, the 3D image acquisition and analysis cost more time and manual work. Therefore, a fast, accurate and automatic method should be developed for acquiring and analysing 3D particle images efficiently.

Effects of ballast particle morphology on performance and deformation

To date, no studies have been reported on the effects of the ballast particle morphology on performance and deformation using the image analysis methods. However, plenty of studies have proved that particle morphology has significant influence on performance and deformation of granular materials (e.g. sands, soils). The early studies on ballast were only using rough indices to evaluate ballast particle morphology, such as the PSD and the Flat or elongated ratio. That is not sufficient to correlate the ballast particle morphology with the performance and deformation. More importantly, rough indices lead to inconclusive test results and controversial conclusions, as discussed in the Sub-section 1.1. Therefore, it is critical to deepen the understanding of the quantitative relation between ballast particle morphology and the performance and deformation. Moreover, according to the accurate and reliable results, it is easier to reveal the mechanism of ballast mechanics.

4.2 Rheology

According to the reviewed studies, the PIV development history can be observed. It started with the displacement measurement, and then was used to measure the velocity and strain. Moreover, it started with recording the displacement/velocity/strain of the target markers, afterwards, it can measure those of the whole sample without target markers. Based on its development history, it shows the feasibility of image analysis for rheology study. More importantly, the PIV developing trend could provide the suggestions and directions for improvement, which are given as follow.

Rotation measurement

It is important to develop the particle rotation measurement with the PIV, because the rotation is a significant aspect of particle rheology study. Whereas almost all studies were focusing on the particle translation, measuring the displacement/velocity/strain. Only one author proposed to utilise the PIV for particle rotation measurement, but the particles were idealized as simple discs. Therefore, further developing the PIV for the rotation measurement of normal particles is promising for particle rheology and rheology-related studies.

Particle morphology

From the reviewed studies on the PIV for railway ballast, the ballast particles were either simplified as prismatic mineral particles or substituted by the 1/3 or 1/5 scaled stones. That is not enough for the ballast rheology study, because the particle shape influences the performance and deformation. Moreover, the rheology is influenced by the gravity and the bulk density, and small particles would usually reach higher compaction.

Track every individual particle

It is more accurate and convictive to study the particle rheology by tracking every individual particle with the PIV, because archiving this could correlate the performance and deformation with the particle rheology at mesoscopic level. The PIV started by tracking the target markers, obviously, the number of tracked particles is not large enough to reflect the ballast particle rheology. Afterwards, the target markers were replaced by tracking the motions of the same or similar pixels on a user-defined area in an image. However, that is still not tracking the displacement/velocity of every individual particles. Therefore, improvements should be made at this aspect for accurate ballast rheology and rheology-related studies.

3D PIV

It is necessary to perform the particle rheology study in 3D, because the particle translation and rotation could be presented veritably by 3D. Currently, the PIV was performed on the 2D basis, in other words, it compares the two or more 2D pictures to measure the displacement/velocity. However, the translation could be at any directions rather than only two certain directions, more inaccurately, when it comes to describing the particle rotation in 2D. Consequently, the PIV could be more beneficial if it could measure the particle displacement/velocity in 3D.

4.3 Degradation

It can be concluded that image analysis can be utilised for particle degradation evaluation from the reviewed studies. More importantly, the developing trend is from 2D to 3D, and from the particle morphology change of whole sample to that of every individual particle. However, the current methods are still not enough to evaluate the particle degradation, and it is not sufficient to correlate that with the performance and deformation. Therefore, the improvement aspects are proposed as below.

From 2D to 3D

One aspect is the estimation of the particle degradation in 3D. Because the particle morphology evaluation in 3D is more promising at high accuracy and resolution and can have more morphological indices e.g. the particle edge (discussed in the sub-section 4.1), while the particle morphology change was utilised in all the introduced degradation evaluation methods.

Particle breakage evaluation

Another aspect is to propose breakage evaluation methods in 3D. Because the fracture surface of a crushed particle is rough, and that could not be estimated clearly based on 2D images. Moreover, the breakage has many types, e.g. breakage at the sharp corner, in the middle or into pieces, which could also not be estimated in 2D. Nevertheless, limited methods for particle breakage evaluation were found, and no methods were reported for the particle breakage evaluation in 3D. Consequently, it is significant to propose a method for particle breakage evaluation in 3D.

Particle degradation mechanism characterisation

It is not sufficient to evaluate ballast degradation only by characterising it as the breakage and abrasion. In [115], degradation is characterised as the wear (surface polishing), fracture (internal breakage), attrition (removal of sharp edges), abrasion (spherical mother particle left), fragmentation (into different fragments) and chipping (removal of chips). However, according to the introductions, most of the image analysis methods evaluate the ballast degradation by quantifying the morphology change from three aspects, the form, angularity and surface texture. Therefore, more studies could be performed on the possibility of image methods to reveal ballast degradation mechanism from more detailed scales.

Particle degradation at experimental tests or in the field

The last aspect is a discussion about the difference of particle degradation between experimental tests and field operation. The reviewed studies mostly utilised the experimental tests (the LAA test or the micro-Deval test) for generating the deteriorated particles, although it was demonstrated in [116] that the degradation trend from the LAA tests could not correlate well with the field. Because the deteriorated ballast particles can be generated by the two tests rapidly, and the different degradation stages are easily controlled by setting different revolution numbers. Whereas, the two tests were mostly used to validate the image analysis methods, and hence using them are sufficient for these purposes.

However, that is not accurate or sufficient to reflect the real particle degradation form. Moreover, using this kind of deteriorated particles to study their performance or deformation is also far from the reality. Most importantly, ballast particle degradation in the field normally costs years. To solve this problem, it is advised to use the cyclic triaxial test or the similar tests, because they are more realistic than the LAA tests or micro-Deval test, easy to control the degradation stages and faster than in the field tests. Therefore, it is more promising and convictive to combine the cyclic triaxial tests (or similar tests) with the image analysis methods for degradation evaluation and degradation-related studies.

4.4 Perspective

After critically reviewing the research and finding the gap, the authors believe that the image analysis has great potential for railway ballast studies, therefore, some possible research directions are proposed as follows:

- Image analysis methods for the whole ballast layer should be considered. The image analysis methods should be used to solve the problems as a final goal, (e.g. ballast degradation mitigation and performance improvement). As a first step, the image-based studies for individual ballast particles have been performed in depth. Afterwards, based on that, the image analysis methods for the performance and deformation of the whole ballast layer should be developed, considering the morphology, rheology and degradation. For instance, the images of Ground Penetration Radar (GPR) may be analysed for detecting the ballast rheology when the train is passing.
- The image analysis could be utilised for exploring the mechanisms of the ballast particle rheology or degradation, and then using the results in the numerical simulations. For more accurate particle morphology presentation in the numerical simulations, the particle images were used to create a shape library in the numerical simulations. However, using the image analysis results of the rheology and degradation in the numerical simulations is relatively unexplored. It is especially interesting to use the mechanisms of the ballast particle rheology or degradation to validate the numerical simulations.
- The image analysis, including for the particle morphology, rheology and degradation, could be combined for systematic railway ballast studies. Image analysis can be applied for studies from the mesoscopic level (surface texture) to the macroscopic scale (deformation). More interestingly, using the images from the satellite can monitor and predict the railway settlement, as proposed in [117]. The combination of these image analysis methods could provide a deeper understanding of some railway ballast problems, differential settlement et. al, and make the progress for solving these kinds of problems.

Acknowledgments

The study is supported by the China Scholarship Council. We would like to thank Ms. Zhang Hong for her correction to this paper, as well as Dr. Elisabeth Bowman, Dr. Janaka J. Kumara, Dr. Olufemi O. Ajayi and Mr. Denis Tunkin for their kind help (the permission of using their thesis figures). We also thank the support of the project of the Rail Infrastructure Systems Engineering Network (RISEN) with the grant number 691135.

Reference

1. Indraratna, B., W. Salim, and C. Rujikiatkamjorn, *Advanced rail geotechnology: Ballasted track*. 2011: CRC press London.
2. Lekarp, F., U. Isacsson, and A. Dawson, *State of the art. I: Resilient response of unbound aggregates.* Journal of transportation engineering, 2000. **126**(1): p. 66-75.
3. Li, D., et al., *Railway geotechnics*. 2002: CRC Press.
4. Vangla, P. and G.M. Latha, *Influence of Particle Size on the Friction and Interfacial Shear Strength of Sands of Similar Morphology.* International Journal of Geosynthetics and Ground Engineering, 2015. **1**(1).
5. Göktepe, A.B. and A. Sezer, *Effect of particle shape on density and permeability of sands.* Proceedings of the Institution of Civil Engineers - Geotechnical Engineering, 2010. **163**(6): p. 307-320.
6. Wang, H., et al., *The effect of morphological characteristic of coarse aggregates measured with fractal dimension on asphalt mixture's high-temperature performance.* Advances in Materials Science and Engineering, 2016. **2016**.
7. Voivret, C., et al., *Multiscale force networks in highly polydisperse granular media.* Phys Rev Lett, 2009. **102**(17): p. 178001.
8. Gates, L., et al., *Aggregate imaging measurement system 2 (AIMS-II): Final Report.* Highway for Life Technology Partnership Program, Federal Highway Administration, US Department of Transportation, 2011.
9. Tafesse, S., J.M.R. Fernlund, and F. Bergholm, *Digital sieving-Matlab based 3-D image analysis.* Engineering Geology, 2012. **137-138**: p. 74-84.
10. Holtz, W. and H.J. Gibbs, *Triaxial shear tests on pervious gravelly soils.* Journal of the Soil Mechanics and Foundations Division, 1956. **82**(1): p. 1-22.
11. Marachi, N.D., C.K. Chan, and H.B. Seed, *Evaluation of properties of rockfill materials.* Journal of Soil Mechanics & Foundations Div, 1900. **97**(SM1).
12. Dunn, C. and P. Bora, *Shear strength of untreated road base aggregates measured by variable lateral pressure triaxial cell.* Journal of Materials, 1972. **7**(2).
13. Ionescu, D., *Evaluation of the engineering behaviour of railway ballast.* 2004.
14. Standard, B., *BS EN 13450 (2002).* Aggregates for railway ballast.
15. Wadell, H., *Volume, shape, and roundness of quartz particles.* Journal of Geology, 1935. **43**(3): p. 250-280.
16. Powers, M.C., *A new roundness scale for sedimentary particles.* Journal of Sedimentary Research, 1953. **23**(2).
17. Galloway, J.E., *Grading, shape, and surface properties.* ASTM special technical publication, 1994. **169**: p. 401-410.
18. Gur, Y., E. Shklarsky, and M. Livneh. *Effect of coarse-fraction flakiness on the strength of graded materials*. in *Asian Conf Soil Mech & Fdn E Proc/Is/*. 1967.
19. Boler, H., Y. Qian, and E. Tutumluer, *Influence of Size and Shape Properties of Railroad Ballast on Aggregate Packing.* Transportation Research Record: Journal of the Transportation Research Board, 2014. **2448**: p. 94-104.

20. Guo, Y., et al., *Ballast degradation: Effect of particle size and shape using Los Angeles Abrasion test and image analysis.* Construction and Building Materials, 2018. **169**: p. 414-424.
21. Erdoğan, S.T., *Determination of aggregate shape properties using X-ray tomographic methods and the effect of shape on concrete rheology*. 2005.
22. Raymond, G.P., *Reinforced ballast behaviour subjected to repeated load.* Geotextiles and Geomembranes, 2002. **20**(1): p. 39-61.
23. Saussine, G., et al., *Modelling ballast behaviour under dynamic loading. Part 1: A 2D polygonal discrete element method approach.* Computer Methods in Applied Mechanics and Engineering, 2006. **195**(19-22): p. 2841-2859.
24. Liu, S., et al., *Comparison of Laboratory Testing Using SmartRock and Discrete Element Modeling of Ballast Particle Movement.* Journal of Materials in Civil Engineering, 2017. **29**(3): p. D6016001.
25. Chen, C., et al., *Discrete element modelling of lateral displacement of a granular assembly under cyclic loading.* Computers and Geotechnics, 2015. **69**: p. 474-484.
26. Voivret, C., et al., *Space-filling properties of polydisperse granular media.* Physical Review E, 2007. **76**(2): p. 021301.
27. Itasca, C., *PFC (particle flow code in 2 and 3 dimensions), version 5.0 [User's manual]*. 2014, Minneapolis.
28. Indraratna, B., et al., *Performance improvement of rail track substructure using artificial inclusions – Experimental and numerical studies.* Transportation Geotechnics, 2016. **8**: p. 69-85.
29. Ngo, N.T., B. Indraratna, and C. Rujikiatkamjorn, *Modelling geogrid-reinforced railway ballast using the discrete element method.* Transportation Geotechnics, 2016. **8**: p. 86-102.
30. Coetzee, C., *Calibration of the discrete element method.* Powder Technology, 2017. **310**: p. 104-142.
31. Mollon, G. and J. Zhao, *3D generation of realistic granular samples based on random fields theory and Fourier shape descriptors.* Computer Methods in Applied Mechanics and Engineering, 2014. **279**: p. 46-65.
32. Wang, Z., et al., *Analysis of ballast direct shear tests by discrete element method under different normal stress.* Measurement, 2015. **63**: p. 17-24.
33. Indraratna, B., P.K. Thakur, and J.S. Vinod, *Experimental and numerical study of railway ballast behavior under cyclic loading.* International Journal of Geomechanics, 2009. **10**(4): p. 136-144.
34. Itasca, C., *PFC 3D-User manual.* Itasca Consulting Group, Minneapolis, 1999.
35. Aikawa, A., *Determination of dynamic ballast characteristics under transient impact loading.* Electron J Struct Eng, 2013. **13**(1): p. 17-34.
36. Indraratna, B., et al., *Compression and degradation of railway ballast under one-dimensional loading.* 1997.
37. Nålsund, R., *Railway ballast characteristics, selection criterion and performance.* Department of Civil and Transport Engineering, Norwegian University of Science and Technology, Trondheim, 2014.
38. Marsal, R.J., *Mechanical properties of rockfill.* Publication of: Wiley (John) and Sons, Incorporated, 1973.
39. Moaveni, M., et al., *Use of Advanced Aggregate Imaging Systems to Evaluate Aggregate Resistance to Breakage, Abrasion, and Polishing.* Transportation Research Record: Journal of the Transportation Research Board, 2014. **2401**: p. 1-10.
40. McDowell, G.R. and H. Li, *Discrete element modelling of scaled railway ballast under triaxial conditions.* Granular Matter, 2016. **18**(3).
41. Saint‐Cyr, B., et al. *Effect of shape nonconvexity on the shear strength of granular media*. in *AIP Conference Proceedings*. 2009. AIP.
42. Tutumluer, E., D. Mishra, and A.A. Butt, *Characterization of Illinois aggregates for subgrade replacement and subbase*. 2009.
43. Greer, M. and M. Heitzman, *Evaluation of the AIMS2 and Micro-Deval to Characterize Aggregate Friction Properties*. 2017.
44. Lu, M. and G. McDowell, *Discrete element modelling of ballast abrasion.* Géotechnique, 2006. **56**(9): p. 651-655.
45. Tunkin, D., *Experimental characterization of the evolution of ballast grain shape and roughness*. 2014, Grenoble INP.
46. Anochie-Boateng, J.K., J.J. Komba, and G.M. Mvelase, *Three-dimensional laser scanning technique to quantify aggregate and ballast shape properties.* Construction and Building Materials, 2013. **43**: p. 389-398.
47. Sneed, E.D. and R.L. Folk, *Pebbles in the lower Colorado River, Texas a study in particle morphogenesis.* The Journal of Geology, 1958. **66**(2): p. 114-150.
48. Krumbein, W.C., *Measurement and geological significance of shape and roundness of sedimentary particles.* Journal of Sedimentary Research, 1941. **11**(2).

49. Wentworth, C.K., *Method of measuring and plotting the shapes of pebbles*. 1923: US Government Printing Office.
50. Sun, Y., B. Indraratna, and S. Nimbalkar Dr, *Three-dimensional characterisation of particle size and shape for ballast.* 2014.
51. Kim, H., et al., *Wavelet-based three-dimensional descriptors of aggregate particles.* Transportation Research Record: Journal of the Transportation Research Board, 2002(1787): p. 109-116.
52. Sympatec, *Windox–operating instructions; Release 5.4. 1.0*. 2008, Sympatec Clausthal-Zellerfeld, Germany.
53. Al-Rousan, T., et al., *Evaluation of image analysis techniques for quantifying aggregate shape characteristics.* Construction and Building Materials, 2007. **21**(5): p. 978-990.
54. Janoo, V., *Quantification of shape, angularity, and surface texture of base course materials*. 1998, Cold regions research and engineering lab hanover nh.
55. Blott, S.J. and K. Pye, *Particle shape: a review and new methods of characterization and classification.* Sedimentology, 2007. **0**(0): p. 070921092734002-???
56. Wenzel, R.N., *Surface roughness and contact angle.* The Journal of Physical Chemistry, 1949. **53**(9): p. 1466-1467.
57. Yemez, Y. and F. Schmitt, *3D reconstruction of real objects with high resolution shape and texture.* Image and Vision computing, 2004. **22**(13): p. 1137-1153.
58. Bujak, B. and M. Bottlinger, *Three‐Dimensional Measurement of Particle Shape.* Particle & Particle Systems Characterization, 2008. **25**(4): p. 293-297.
59. Hayakawa, Y. and T. Oguchi, *Evaluation of gravel sphericity and roundness based on surface-area measurement with a laser scanner.* Computers & Geosciences, 2005. **31**(6): p. 735-741.
60. Kuo, C.-Y., et al., *Three-dimensional image analysis of aggregate particles from orthogonal projections.* Transportation Research Record: Journal of the Transportation Research Board, 1996(1526): p. 98-103.
61. Okonta, F., *Effect of grading category on the roundness of degraded and abraded railway quartzites.* Engineering Geology, 2015. **193**: p. 231-242.
62. Palasamudram, S. and S. Bahadur, *Particle characterization for angularity and the effects of particle size and angularity on erosion in a fluidized bed environment.* Wear, 1997. **203**: p. 455-463.
63. Clark, M.W., *Quantitative shape analysis: a review.* Journal of the International Association for Mathematical Geology, 1981. **13**(4): p. 303-320.
64. Barksdale, R.D., et al., *Measurement of aggregate shape, surface area, and roughness.* Transportation Research Record, 1991(1301).
65. Bowman, E.T., K. Soga, and T.W. Drummond, *Particle shape characterisation using Fourier analysis*. 2000: University of Cambridge, Department of Engineering.
66. Hyslip, J.P. and L.E. Vallejo, *Fractal analysis of the roughness and size distribution of granular materials.* Engineering geology, 1997. **48**(3-4): p. 231-244.
67. Mora, C. and A. Kwan, *Sphericity, shape factor, and convexity measurement of coarse aggregate for concrete using digital image processing.* Cement and concrete research, 2000. **30**(3): p. 351-358.
68. Sukumaran, B. and A. Ashmawy, *Quantitative characterisation of the geometry of discret particles.* Geotechnique, 2001. **51**(7): p. 619-627.
69. Tong, Z., J. Gao, and H. Zhang, *Innovation for evaluating aggregate angularity based upon 3D convolutional neural network.* Construction and Building Materials, 2017. **155**: p. 919-929.
70. Kuo, C.-Y. and R. Freeman, *Imaging indices for quantification of shape, angularity, and surface texture of aggregates.* Transportation Research Record: Journal of the Transportation Research Board, 2000(1721): p. 57-65.
71. Zhang, D., X. Huang, and Y. Zhao, *Investigation of the shape, size, angularity and surface texture properties of coarse aggregates.* Construction and Building Materials, 2012. **34**: p. 330-336.
72. Fernlund, J.M., R.W. Zimmerman, and D. Kragic, *Influence of volume/mass on grain-size curves and conversion of image-analysis size to sieve size.* Engineering geology, 2007. **90**(3-4): p. 124-137.

73. Brzezicki, J.M. and J. Kasperkiewicz, *Automatic image analysis in evaluation of aggregate shape.* Journal of computing in civil engineering, 1999. **13**(2): p. 123-128.
74. Kumara, G.H.A.J.J., *Development of prediction methods for deformation characteristics of fouled ballasts based on laboratory experiments and discrete element method*. 2013, 横浜国立大学.
75. Tolppanen, P., *3-D Characterization and Degradation Analysis of Rock Aggregates*. 2001, Institutionen för anläggning och miljö.
76. Erdogan, S., et al., *Three-dimensional shape analysis of coarse aggregates: New techniques for and preliminary results on several different coarse aggregates and reference rocks.* Cement and Concrete Research, 2006. **36**(9): p. 1619-1627.
77. Sukumaran, B. and A.K. Ashmawy, *Influence of inherent particle characteristics on hopper flow rate.* Powder Technology, 2003. **138**(1): p. 46-50.
78. Wnek, M., et al., *Investigation of Aggregate Properties Influencing Railroad Ballast Performance.* Transportation Research Record: Journal of the Transportation Research Board, 2013. **2374**: p. 180-189.
79. Lanaro, F. and P. Tolppanen, *3D characterization of coarse aggregates.* Engineering Geology, 2002. **65**(1): p. 17-30.
80. Wettimuny, R. and D. Penumadu, *Application of Fourier analysis to digital imaging for particle shape analysis.* Journal of Computing in Civil Engineering, 2004. **18**(1): p. 2-9.
81. Wang, L., et al., *Unified method to quantify aggregate shape angularity and texture using Fourier analysis.* Journal of Materials in Civil Engineering, 2005. **17**(5): p. 498-504.
82. Garboczi, E.J., *Three-dimensional mathematical analysis of particle shape using X-ray tomography and spherical harmonics: Application to aggregates used in concrete.* Cement and concrete research, 2002. **32**(10): p. 1621-1638.
83. Le Pen, L.M., et al., *Dependence of shape on particle size for a crushed rock railway ballast.* Granular Matter, 2013. **15**(6): p. 849-861.
84. Masad, E., et al., *Correlation of fine aggregate imaging shape indices with asphalt mixture performance.* Transportation Research Record: Journal of the Transportation Research Board, 2001(1757): p. 148-156.
85. Lees, G., *A new method for determining the angularity of particles.* Sedimentology, 1964. **3**(1): p. 2-21.
86. Fletcher, T., et al., *Measurement of aggregate texture and its influence on hot mix asphalt (HMA) permanent deformation.* Journal of testing and evaluation, 2002. **30**(6): p. 524-531.
87. Browne, C., et al., *Performance evaluation of automated machines for measuring gradation of aggregates.* Geotechnical Testing Journal, 2003. **26**(4): p. 373-381.
88. Kim, H., et al., *Dimensional ratios for stone aggregates from three-dimensional laser scans.* Journal of computing in Civil Engineering, 2002. **16**(3): p. 175-183.
89. Kuo, C.-Y., *Correlating permanent deformation characteristics of hot mix asphalt with aggregate geometric irregularities.* Journal of testing and evaluation, 2002. **30**(2): p. 136-144.
90. Tolppanen, P., O. Stephansson, and L. Stenlid, *3-D degradation analysis of railroad ballast.* Bulletin of Engineering Geology and the Environment, 2002. **61**(1): p. 35-42.
91. Qian, Y., et al., *Degradation-Related Changes in Ballast Gradation and Aggregate Particle Morphology.* Journal of Geotechnical and Geoenvironmental Engineering, 2017. **143**(8): p. 04017032.
92. Sekine, E., A. Kono, and A. Kito, *Strength and deformation characteristics of railroad ballast in ballast particle abrasion process.* Quarterly Report of RTRI, 2005. **46**(4): p. 256-261.
93. Mahmoud, E. and E. Masad, *Experimental methods for the evaluation of aggregate resistance to polishing, abrasion, and breakage.* Journal of Materials in Civil Engineering, 2007. **19**(11): p. 977-985.
94. Tutumluer, E., *Field Imaging Based Assessment of In-Service Ballast Condition.* Urbana, 2016. **51**: p. 61801.
95. Fernlund, J., *3-D image analysis size and shape method applied to the evaluation of the Los Angeles test.* Engineering geology, 2005. **77**(1): p. 57-67.
96. Gaitskell, P. and M. Shahin, *Use of digital imaging for gradation and breakage of railway ballast.* Australian Geomechanics, 2013. **48**(3): p. 81-88.
97. Souza, L.T. and Y. Kim, *Effects of Aggregate Angularity on Mix Design Characteristics and Pavement Performance.* 2009.

98. Sun, W., *Quantification of Morphological Characteristics of Aggregates at Multiple Scales*. 2015, Virginia Tech.
99. Swift, G.A., *Characterization of coarse aggregate angularity using digital image processing.* 2007.
100. Adrian, R.J., *Particle-imaging techniques for experimental fluid mechanics.* Annual review of fluid mechanics, 1991. **23**(1): p. 261-304.
101. White, D., et al. *A deformation measurement system for geotechnical testing based on digital imaging, close-range photogrammetry, and PIV image analysis*. in *Proceedings of the International Conference on Soil Mechanics and Geotechnical Engineering*. 2001. AA Balkema Publishers.
102. NI, Q., C. Hird, and I. Guymer, *Physical modelling of pile penetration in clay using transparent soil and particle image velocimetry.* Géotechnique, 2010. **60**(2): p. 121-132.
103. Zhao, H. and L. Ge, *Camera calibration using neural network for image-based soil deformation measurement systems.* Geotechnical Testing Journal, 2007. **31**(2): p. 192-197.
104. Hryciw, R.D. and M. Irsyam, *Behavior of sand particles around rigid ribbed inclusions during shear.* Soils and foundations, 1993. **33**(3): p. 1-13.
105. Alshibli, K.A. and S. Sture, *Shear band formation in plane strain experiments of sand.* Journal of Geotechnical and Geoenvironmental Engineering, 2000. **126**(6): p. 495-503.
106. Rechenmacher, A.L. and R.J. Finno, *Digital image correlation to evaluate shear banding in dilative sands.* Geotechnical Testing Journal, 2003. **27**(1): p. 13-22.
107. Boldyrev, G., A. Melnikov, and V. Barvashov. *Particle Image Velocimetry and Numeric Analysis of Sand Deformations under a Test Plate*. in *The 5th European Geosynthetics Congress*. 2012.
108. Mel'nikov, A. and G. Boldyrev, *Deformation Pattern of Sand Subject to Static Penetration.* Soil Mechanics and Foundation Engineering, 2015. **51**(6): p. 292-298.
109. Paikowsky, S.G. and F. Xi, *Particle motion tracking utilizing a high-resolution digital CCD camera.* Geotechnical Testing Journal, 2000. **23**(1): p. 123-134.
110. Sevi, A.F., L. Ge, and W.A. Take, *A large-scale triaxial apparatus for prototype railroad ballast testing.* Geotechnical testing journal, 2009. **32**(4): p. 297-304.
111. Ajayi, O., et al., *A behavioural framework for fibre reinforced gravel.* Géotechnique, 2016: p. 1-35.
112. Bhandari, A., W. Powrie, and R. Harkness, *A digital image-based deformation measurement system for triaxial tests.* Geotechnical Testing Journal, 2011. **35**(2): p. 209-226.
113. Hayano, K., K. Ishii, and K. Muramoto. *Effects of ballast thickness and tie-tamper repair on settlement characteristics of railway ballasted tracks*. in *Proceedings of the 18th International Conference on Soil Mechanics and Geotechnical Engineering*. 2013.
114. Liu, H., et al., *Experimental investigation of the characteristics of a granular ballast bed under cyclic longitudinal loading.* Construction and Building Materials, 2018. **163**: p. 214-224.
115. Van Laarhoven, B., *Breakage of Agglomerates: Attrition, Abrasion and Compression.* 2010.
116. Moaveni, M., et al., *Morphological Characterization of Railroad Ballast Degradation Trends in the Field and Laboratory.* Transportation Research Record: Journal of the Transportation Research Board, 2016. **2545**: p. 89-99.
117. Chang, L., R.P. Dollevoet, and R.F. Hanssen, *Nationwide railway monitoring using satellite SAR interferometry.* IEEE Journal of Selected Topics in Applied Earth Observations and Remote Sensing, 2017. **10**(2): p. 596-604.
118. Mahmoud, E., et al., *Comprehensive evaluation of AIMS texture, angularity, and dimension measurements.* Journal of Materials in Civil Engineering, 2009. **22**(4): p. 369-379.
119. Rajan, B. and D. Singh, *Understanding influence of crushers on shape characteristics of fine aggregates based on digital image and conventional techniques.* Construction and Building Materials, 2017. **150**: p. 833-843.
120. Moaveni, M., et al., *Evaluation of Aggregate Size and Shape by Means of Segmentation Techniques and Aggregate Image Processing Algorithms.* Transportation Research Record: Journal of the Transportation Research Board, 2013. **2335**: p. 50-59.
121. Al Rousan, T.M., *Characterization of aggregate shape properties using a computer automated system*. 2005, Texas A&M University.

122. Descantes, Y., Y. Fosse, and F. Milcent, *Automated measurement of railway ballast angularity.* Journal of materials in civil engineering, 2006. **18**(4): p. 612-618.

123. Rauch, A.F., et al., *Rapid Test to Establish Grading of Unbound Aggregate Products: An Evaluation of Automated Devices to Replace and Augment Manual Sieve Analyses in Determining Aggregation Gradation*. 2002.

124. Rodriguez, J., *Particle shape quantities and influence on geotechnical properties: a review*. 2012.

125. Chekirad, M. and V. Roubtsova, *Influence of Particles Shape, Size and Uniformity of sands on the Void Ratio Range and Consequently on the Dynamic Penetration Tests Results.*

126. Ohm, H.-S., *Image-Based Soil Particle Size and Shape Characterization.* 2013.

127. Pentland, A., *A method of measuring the angularity of sands.* Proceedings and Transactions of the Royal Society of Canada, 1927. **21**(3): p. 43.

128. Clayton, C., C. Abbireddy, and R. Schiebel, *A method of estimating the form of coarse particulates.* Geotechnique, 2009. **59**(6): p. 493-501.

129. Aschenbrenner, B.C., *A new method of expressing particle sphericity.* Journal of Sedimentary Research, 1956. **26**(1): p. 15-31.

130. Williams, E.M., *A method of indicating pebble shape with one parameter.* Journal of Sedimentary Research, 1965. **35**(4).

131. Dobkins Jr, J.E. and R.L. Folk, *Shape development on Tahiti-nui.* Journal of Sedimentary Research, 1970. **40**(4).

132. Ouhbi, N., et al., *3D particle shape modelling and optimization through proper orthogonal decomposition.* Granular Matter, 2017. **19**(4): p. 86.

133. Laughlin, G.R., *Limestone fine aggregate in Portland cement concrete.* 1960.

134. Kuenen, P.H., *Experimental abrasion of pebbles I. Wet sandblasting.* Leidse Geol. Mededel, 1956. **20**: p. 131-137.

135. Swan, B., *Measures of particle roundness: a note.* Journal of Sedimentary Research, 1974. **44**(2).

136. Pan, T. and E. Tutumluer, *Imaging-based direct measurement of aggregate surface area and its application in asphalt mixture design.* International Journal of Pavement Engineering, 2010. **11**(5): p. 415-428.

137. Ozen, M. and M. Guler, *Assessment of optimum threshold and particle shape parameter for the image analysis of aggregate size distribution of concrete sections.* Optics and Lasers in Engineering, 2014. **53**: p. 122-132.

Table 3 Photography analysis (SIA) with 2D output

Reference	Apparatus	Raw data	Study highlights	Output				
				Form	Angularity	Surface texture	Size	Degradation
Clark, 1981	Camera	Unique image of particle	1. Reviewed and summarised three methods for unrolling the particle outline, as explained at the Fourier series.	-	-	-	-	-
Janoo, 1998	Camera	Unique image of particles	1. Summarised the direct methods (image analysis) of form, angularity and surface texture evaluation, and the index tests (indirect methods, e.g. pouring test) for the combination of the three shape characteristics evaluation. 2. Reviewed studies of effects of the three characteristics on the base course performance. 3. Given the prospective of the combined effects of particle shape, fines content and moisture on base course performance.	Circularity	Angularity index or Roundness	Roughness	-	-
Palasamudram & Bahadur, 1997	-	Unique image of particle	The proposed angularity evaluation method considers the sharpness of particle corners and the probability of these corners contacting the target surface.	-	Angularity index	-	-	-
Hyslip & Vallejo, 1997	Camera	Unique image of particles	Fractal dimensioning technique (parallel-line method) is proposed to evaluate the particle surface texture and size (further particle size distribution, PSD). The PSD of well-graded granular soils can be quantified accurately.	-	-	Fractal dimension	Fragmentation fractal dimensioning	-
Brzezicki et al., 1999	Camera; Particles placed on perpendicular walls	Unique image of particles	Single particle projection and two shadows of the particle (in one image) are used to evaluate three dimensions of the particle.	Flat or Elongated ratio	-	-	-	-
Bowman et al., 2000	Scanning electron microscope	Unique image of particles	The Fourier descriptor method is used to solve the problem when the particle outline has a concave shape and has two possible *r(θ)* value. Moreover, the Fourier descriptor is utilised to describe the particle shape, and the surface texture.	Fourier descriptor method	Fourier descriptor method	Fourier descriptor method for surface texture	-	-
Kuo & Freeman, 2000	Camera; Particles placed on adhesive transparent	Two perpendicular projections of particles	1. The adhesive Plexiglas tray with two perpendicular walls are used for capturing two perpendicular projections of one particle. 2. The image-based morphological indices of particles correlates well to the effects of particle shape characteristics on hot-mix asphalt concrete mixtures. 3. The particle intermediate axe is utilised as the particle size instead of	Form index and Aspect ratio	Angularity index or Roundness	Roughness	Particle intermediate axe as particle size	-

	plastic trays with two perpendicular faces		the sieve size.					
Mora et al., 2000	Quantimet Q600 image analyser, with 3-chip CCD video camera and a frame grabber with three A/D converters	Unique image of particles	The analyser can measure image characteristics such as area, perimeter and size distribution. The proposed image analysis method can estimate the thickness and volume of the particles. After comparing the earlier angularity evaluation methods with the proposed convexity ratio and fullness ratio, it is found the convexity ratio and fullness ratio can be used for angularity evaluation. 2. The particle size distribution is presented with the percentages by particle area on a stable horizontal surface (area gradation).	Sphericity; Flaky or elongated ratio; Shape factor	Convexity ratio and Fullness ratio	-	Volume; Area gradation	-
Sukumaran & Ashmawy, 2001, 2003	Quantimet 570 image analyser;	Unique image of particles	The analyser can measure image characteristics such as area, perimeter and size distribution. It is demonstrated that the shape characteristics has strong correlation with the drained friction angle and void ratio and the measured maximum or minimum void ratio, further, the flow rate through a flow cone (hopper).	Form index	Angularity index	-	-	-
Wettimuny et al., 2004	Camera; Laser scanning confocal microscope	Two perpendicular projections of particle; 2D contours	The Summation of the square of residual (TSSR; see Table 8), another Fourier series method analysing 2D particle images, is calculated based on the cumulative error (amplitude of the radial vector) between the reconstructed particle profile and the original one.	Form index	-	Roughness factor	-	-
Wang et al., 2005	Camera	Unique image of particle	By the ratio of the reconstructed and original profile areas, the Particle signature is determined. Particle signature at different ranges of frequency are used for the quantification of form, angularity and surface texture. It needs to be noted that this method allows more definitive physical interpretation of the particle's profile features, by using Particle signature at different ranges of frequency.	Form index	Angularity index	Surface texture index	-	-
Sekine et al., 2005	Camera	-	After the LAA tests generating deteriorated ballast particles, the triaxial test and the cyclic loading test (upon a large-scale track model) are performed to study the performance and deformation of ballast particles at different degradation stages. The degradation stages are quantified using the morphological indices from Fourier series. The results show a correlation between the degradation stages and the particle performance or deformation (stiffness, strength and settlement), and demonstrate that the Fourier series method is effective and objective.	Aspect ratio	Angularity index	-	-	Degradation quantification with Fourier series

Zhang et al., 2012	Camera	Two images of particles	The morphological index, Angularity and Surface texture (AT) index is proposed to characterise the combined effect of the particle angularity and surface texture.	-	Angularity index and the Surface texture index	Angularity index and the Surface texture index	-	-
Ozen & Guler, 2014	Desktop flatbed scanner	The scanned images were recorded in grey scale format	After comparing three methods (right side) for particle size distribution evaluation, the maximum ferret diameter is the most suitable size parameter to evaluate particle size distributions.	-	-	-	Equivalent ellipse major axis, particle area and Maximum ferret diameter for particle size distribution	-

Note: the mark "-" presents not mentioned or not studied in the reference article.

Table 4 Photography analysis with 3D output

Reference	Apparatus	Raw data	Study highlights	Output				
				Form	Angularity	Surface texture	Size	Degradation
Barksdale et al., 1991	Pencept Penpad digitizer, scanning electron microscope	Unique image of particles	The particle shadow is utilised to calculate particles thickness (the shortest axe).	Form index; Sphericity	-	Roughness	-	-
Kuo et al., 1996	Quantimet Q570 Image Analysis System; Particles placed on	Two perpendicular projections of particles	3D analysis for particles was performed by attaching particles in sample trays with two perpendicular walls for obtaining three axes of the particles.	Sphericity; Flat or Elongated ratio	Roundness; Fullness ratio	-	-	-

	adhesive transparent plastic trays with two perpendicular faces							
Fernlund, 2005, 2007	Camera	Two images of particles (maximum and minimum projected area of the particles)	1. With the image-based particle size and shape distribution, the ballast degradation is evaluated by comparing the distribution change.	Flat or Elongated ratio; Zingg's classification	-	-	All three axes of all the particles	PSD change; Flat or elongated ratio change
Clayton et al., 2009	Leica Z16APO monocular microscope fitted with a SIS/Olympus CC12 colour camera	Three projected images of particles in three-orthogonal directions	1. After reviewed earlier studies on form, it demonstrates that many proposed measures are 2D and therefore not well suited to the particle shape evaluation. 2. An image-based morphological index for form evaluation is proposed, which is according to the smallest dimension of a scalene ellipsoid with the same volume as the given particle, and the method of measuring it using static imaging is introduced.	Scalene Ellipsoid Equivalent Sphericity	-	-	-	-
Le Pen et al., 2013	Camera	Two different orthogonal projections of particle	1. Developed the Ellipseness, a morphological index, for evaluating and quantifying particle shape. 2. Presented that there are measurable and quantifiable differences (although small) in particle shape with size.	Scalene Ellipsoid Equivalent Sphericity, Zingg's classification	Ellipseness	-	-	-
Okonta et al., 2015 [61]	CCD video camera	Unique image of particles	Two different PSDs of ballast samples are performed LAA tests. Results show that the morphology affected the degradation degree differently, and with the LAA loss decreasing, mean roundness becomes increasingly dependent on both the effect of degradation and grading. This demonstrates the potentiality of using image analysis (digital images) for degradation evaluation and quantification.	-	Roundness	-	-	Mean Roundness change

1154

1155 *Table 5 Image analysis systems*

Reference	Apparatus	Raw data	Study highlights	Output				
				Form	Angularity	Surface texture	Size	Degradation

Masad et al., 2011	Aggregate Image Measurement System (AIMS); second generation of Aggregate Image Measurement System (AIMS2)	One high-resolution grey image and one black and white image of particle projections	Apparatuses: the AIMS consists of independent software for characterising particle shape and a computer-controlled system (particle image acquisition). It is equipped with a camera connected with a video microscope (for auto focus), three closed-loop DC servo motor linear actuators, a particle tray and a backlighting table, as shown in figure below. The three actuators are utilised for independent and simultaneous precision movement along three coordinate-axes. The second generation of Aggregate Image Measurement System (referred as AIMS2) is more advanced, which is equipped with two lighting configurations (back lighting and top lighting) and a microscope-camera system enclosed in a box, isolating particles from the outside light sources, as shown in figure below. Besides the lighting improvements, the rotating tray is used to align each particle directly under the camera to ensure that each particle is in full view for the better image acquisition. Both the AIMS and the AIMS2 rank the particle sources the same among every morphological indices and provide comparable results, as reported in [43]. Raw data process: the developed user-friendly software is used to analyse the captured images and can evaluate form, angularity and surface texture for both fine and coarse aggregates.	Circularity; Form index; Flat or Elongated ratio; Aspect ratio; Sphericity; From index	Radius method; Gradient method; Surface Erosion-Dilation technique	Surface Erosion-Dilation technique; Wavelet transform	-	Surface texture index change; Angularity index change

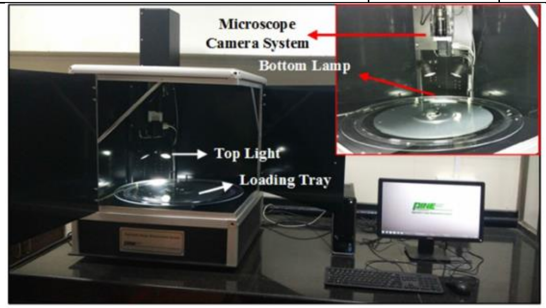

AIMS (left; reproduced from [118]) and AIMS2 (right; reproduced from [119])

Tutumluer & Rao, 2000, 2009 [42]	University of Illinois Aggregate Image Analyzer (UIAIA); Enhanced-University of Illinois Aggregate Image Analyzer (E-UIAIA)	Three orthogonal images of particle	The UIAIA uses 3 cameras from three orthogonal directions to obtain images. The E-UIAIA is later developed with high-resolution, progressive-scan digital colour cameras. The E- UIAIA is different from the first version (using black-and-white images). By enhancing this together with an advanced colour-thresholding scheme, the E-UIAIA can scan various type of mineral particles [120]. The UIAIA and E-UIAIA can provide more accurate evaluation of the particle shape by calculating the morphological indices with the weighted average of the indices at the three directions automatically. The morphological indices include the Flat and elongated ratio, Angularity index, Surface texture index, Surface area and Volume. Raw data process: The National Instruments LabVIEW™ software and the inserted image analysis package IMAQ Vision library is utilised for performing the necessary	Flat & elongated ratio	Angularity index	Surface texture index	Volume; Surface area	Morphological indices change

			user-programmed functions to capture and analyse particle images. The UIAIA operating software includes the following functions: image acquisition, particle volume computation, particle size, particle angularity calculation, and surface texture evaluation.					
	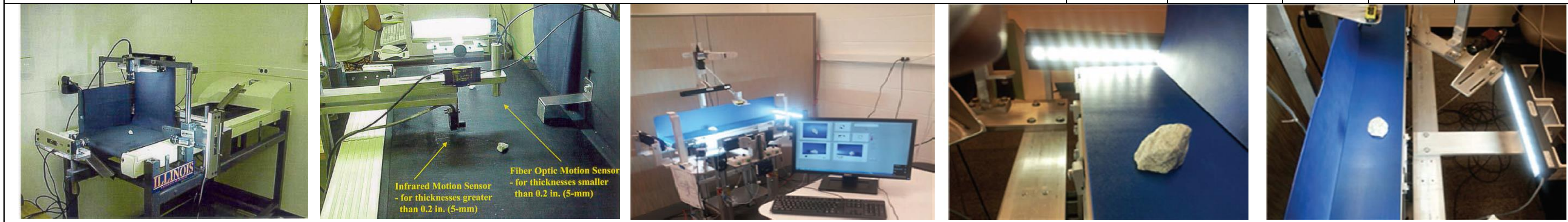 *Components of the UIAIA system and details of aggregate detection system (left; reproduced from [121]); E-UIAIA system (right; reproduce from [120])*							
Kim et al., 2002	Laser-Based Aggregate Scanning System (LASS)	Upper side 3D image of particles	The Laser-based Aggregate Scanning System (LASS) can solve the problem by obtaining and analysing the 3D particle images. A laser scanner (linear motion slide) passes over the particles with a beam of light spreading out on a platform, as shown in figure below. The scanner captures the coordinates of the points of the laser stripe on the surface. It has a 120 mm scanning width, which means that if the particles are spread within 120 mm, simultaneous scanning of multiple particles is possible. With the resolution at about 0.5 mm in three orthogonal directions, the LASS can scan 15 particles per second, if the particles are smaller than 10 mm (longest axe). The LASS analyses the 3D particle images with higher accuracy, however, it only scans the upper surfaces of the particles. Therefore, the LASS can be considered as the method between 2D and 3D image analysis. Raw data process: The software is written with the IMAQ Vision image processing tool, which is developed by National Instruments. It converts the obtained data into a 2D image and the processing algorithms are utilised to evaluate particle shape from the image, due to the computational efficiency. It also provides almost complete 3D information of every particles, by storing the height data of every particles separately, so that the full 3D data are saved while the 2D image processing techniques are applied to the obtained images. The half 3D images are transformed into grey-scale digital images. Grey-scale pixels determine the height of each datum point.	Form index	Angularity index	Surface texture index	Volum e	-

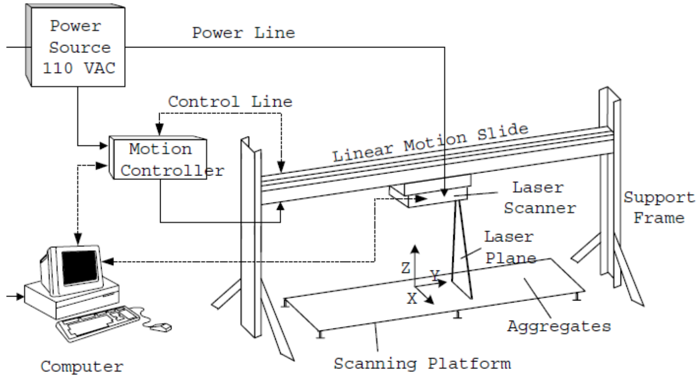

Laser-based aggregate scanning system (figure reproduced from [51])

Lanaro, 2001	3D laser-digitising system	3D image of particle	The 3D laser-digitising system evaluates the particle shape with the Fourier series or the geometrical methods (Cylindrical encompassing method and the Parallel-plane encompassing method). The laser scanner is used to measure the coordinates of the particles by moving along three orthogonal directions. Raw data process: After the particle is scanned, data of its upper and lower sides are saved as the point clouds. The images of the two sides are combined to form a complete 3D particle image. The Fast Fourier series are used for particle shape evaluation based on the rectangular coordinates, when combined with the power spectrum analysis. This method analyses the cross-sections of the 3D particle image, and it is explained at the Analytical Fourier analysis (Lanaro, 2001).	Particle shape categories	-	Roughness	Volume	Degradation index

Anochie-	3D Laser scanning device at CSIR	3D image of particle	The device utilises the laser scanner to scan particles in three dimensions and its resolution can be up to a 0.1mm. A combination of precision optics and motion control	Sphericity; Flat	-	-	Volume;	-

Boateng et al., 2012, 2013			with a rigid cast aluminium frame produces high quality scanning of particles. It is able to scan with rotary or plane scanning modes, which is suitable for particles of various types and sizes. Raw data process: the inserted software can combine and merge the scanned surfaces to obtain the complete particle, and then directly obtaining the longest, intermediate and shortest axes of a particle. The surface area and the volume of the particle can be also computed with the inserted software. More importantly, it is proved in [46] that the results of the particle volume and surface area agree quite well with numerical computations. The particle volume can reach the excellent correlation (R^2 = *0.9994*), while the particle surface area has the difference value within 10^{-5} mm^2.	and elongate ratio;			Surface area	

Table 6 Other image analysis methods

Reference	Apparatus	Raw data	Study highlights	Output				
				Form	Angularity	Surface texture	Size	Degradation
Hayakawa et al., 2005	3D Scanner	3D image of particle	The device is the same product as the 3D Laser scanning device at CSIR in Table 5. As shown in figure below, two images of the particle with diverse orientations are aligned and merged with the software, PixForm 1.0. With geometrical properties of the 3D image, two morphological indices, i.e. the Modified Wadell's Sphericity and Roundness are utilised for the quantification of the form and the angularity, respectively.	Modified Wadell's Sphericity	Roundness	-	Volume; Surface area	-

			The Sphericity illustrates a surprisingly high association with Krumbein's Roundness, notwithstanding Sphericity and Roundness are regarded as the morphological indices for form and angularity, respectively. The new morphological index (modification of the true sphericity) is proposed to show the differences of particle shape from an ellipsoid that has given axe lengths. This morphological index shows little correlation with Roundness and particle size.					

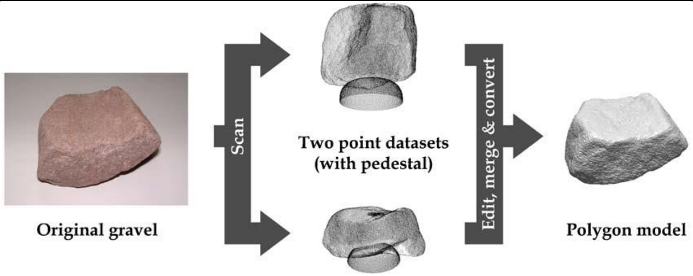

3D particle image acquisition (reproduced from [59])

Ouhbi et al., 2017	3D scanner	3D Surface points of particle	After the 3D scanning, around 300,000 surface points for one particle are obtained. The 3D scanner was not described in details in their research paper. Raw data process: normal aim of the proper orthogonal decomposition (POD) is extracting the dominant features from the total data, afterwards building a simplified model. Here, the method utilises the method for enabling shape description with a controlled accuracy.	Form index	-	-	-	-
Sun et al., 2014	3D laser scanner (VIVID 910)	3D image of particle	The specific description of the device is not mentioned in their paper. The study utilises the three dimensions and surface area of the particle to calculate the morphological index. A morphological index for form evaluation is proposed. Raw data process: the computer software Geomagic Qualify 12 (version 15.0) is utilised for the raw data process, including, forming the 3D triangulate model, restoring the small holes and eliminating the noises. The surface area of the particle is computed by summing up all the triangles' area, while the volume is calculated by summing up all the sub-volumes of the tetrahedral mesh, which are the same methods that are mentioned in the Anochie-Boateng's study.	-	Ellipsoidness	-	Volume; surface area	-
Garboczi et al., 2002	X-ray CT scanner	3D image of particle	For the 3D images, the Spherical harmonics series (Fourier series method) is utilised for reconstructing and quantifying the particle shape according to measurements performed on the 3D images [82].	-	-	-	Volume; surface area	-
Erdoğan et al., 2006	X-ray CT scanner	Reconstructed 3D image of particle	2D images from X-ray can be reconstructed to form the 3D image with appropriate algorithms, which is the spherical harmonic reconstruction.	Flat or Elongated ratio	-	-	-	-

Tunkin & Denis, 2014	X-ray CT scanner; laser displacement sensor	Reconstructed 3D image of particle; a face of particle	The main components of X–ray CT scanner include the X– ray generator, detector and rotation stage, which are put into a large box. The 2D images at different angular positions reconstruct the 3D image of the particle with appropriate algorithms. The abraded parts after tests can be seen after aligning and comparing the 2D images together with transforming the 2D images into 3D ones. The laser displacement sensor uses the direct reflected light of a red laser beam for obtaining the distance to the surface by measuring the light traveling time. Raw data process: the particle form and angularity are analysed with the Spherical harmonics series. The spherical harmonic coefficients utilised for the form and angularity are 5 and 25, respectively.	Sphericity; Flat or Elongated ratio; Form index	Angularity index	Several indices are given in [45]	-	Abraded part of particle; changes of morphological indices
Guo et al., 2018	3D scanner	3D image of particle	A particle is placed on a black turntable, which can spin during scanning process to get images of every particle side. The blue light reflected from particle surface is captured by coupled device camera. About 500,000 vertices are transmitted to the computer, and three consequent images are used to form one triangular plane. Finally, all small triangular planes constitute the 3D ballast particle image. Raw data process: the two particle images before and after LAA test are aligned and compared for checking the differences. In addition, the volume change is also checked in this study.	Sphericity	-	-	Volume; surface area	Degradation evaluation by 3D image difference

Table 7 Dynamic image analysis methods

Reference	Apparatus	Raw data	Study highlights	Output				
				Form	Angularity	Surface texture	Size	Degradation
Descantes, et al., 2006 [122]	VDG40 Videograder	Unique projection of particle	As shown in figure below (reproduced from [122]), the VDG40 is developed by the Laboratoire Central des Ponts et Chaussees (LCPC). It consists of an apparatus to feed the particles (passing the backlight), and a line-scan CCD camera to capture particle images. The CCD camera has a resolution of 1,024 dots and a 13 kHz scan frequency. The VDG-40 can be sued for measuring granular materials, whose size ranges are from 1.18 mm to 38.1 mm. Raw data process: the algorithm (assuming particles are elliptical) is utilised to compute each particle's three axes with the 2D projection.	Shape Class Average Ratio (SCAR)	Angularity index	Surface texture index	Particle size distribution; volume	Angularity index change

	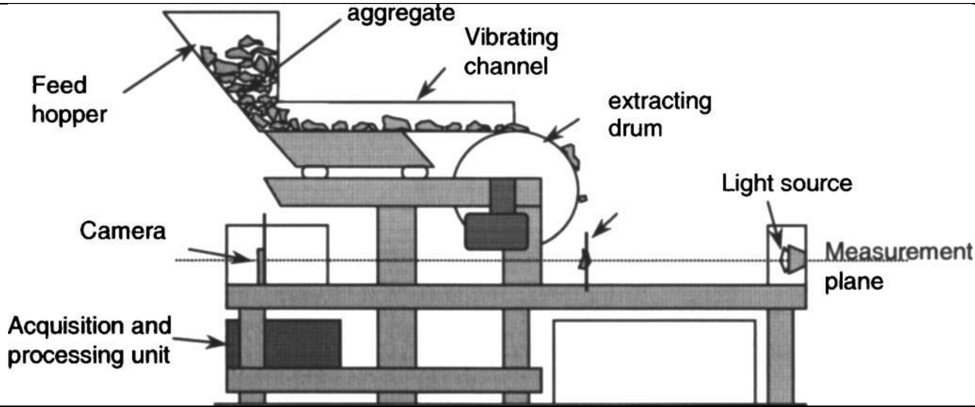							
Rauch et al., 2002 [123]	Micrometrics OptiSizer System	Unique image of particles	This apparatus was originally developed for online measurements. It utilises a matrix CCD camera to photograph and evaluate particles when falling in front of the backlight (about twice per second). The particle sizes that can be measured are from a No. 200 mesh sieve size (0.075 mm) up to at least 1.5 inch (38.1 mm). Like the above DIA system, an idealized shape of particles is used to provide information about particle size distribution and shape. Raw data process: The spherical type analysis converts each imaged particle profile area into a circle with equal area. The volumetric information is calculated with the radius of the circle as a sphere volume. The cubic analysis converts particle profile area into a square with equal area. The volume information is then calculated as a cube with the side dimension of the square.	Spherical analysis; cubic analysis	-	-	Volumetric information	-
Rauch et al., 2002 [123]	Video Imaging System	Unique image of particles	The Video Imaging System (VIS) is developed for on-line particle measurements. It is designed to combine the Micrometrics OptiSizer System with the developed conveyor belt sweep samplers. It can analyse particles from 1.18 mm sieve to 38.1 mm. Raw data process: it is not described in details in the literature.	Yes	-	-	Yes	-
Rauch et al., 2002 [123]	Buffalo Wire Works System Particle Size Distribution Analyzer (PSDA)	Unique image of particle	The PSDA utilises vibratory feeder to create a curtain of backlit and a progressive matrix CCD camera. It does not take all the particles' images in the sample. It can automatically adjust the camera focus and optimise the backlight according to the settings for various particle size ranges. It can measure particles ranging from 0.075 to 38 mm. After the samples are put into the vibratory	Form index			Yes	-

			feeder, the computer controls the measuring process. It has the unique feature that is the automatic measurement stops once enough data for the correct PSD have been obtained. Raw data process: the proprietary software is utilised to obtain the size and shape.					
Browne et al., 2002 [87]	Computer Particle Analyser (CPA)	Unique projection of particle	Like the VDG40, the CPA utilises a line-scan CCD camera to photograph each particle in the sample when they are falling in front of a backlight. Particle size is tabulated as a function of particle count, afterwards a simple correlation factor is utilised to transform the data into the volume gradation. Three different version of CPA can measure three different particle size ranges. The CPA-4 analyses particle size up to 600 mm in size. Raw data process: the proprietary software is utilised to obtain the size and shape.	Flat or elongated ratio	-	-	Size method; shape method	-
Rauch et al., 2002 [123]	Camsizer	Two images of particle	The Camsizer system uses two cameras to photograph images at different resolutions. It measures the particles in the sample when they are falling in front of a backlight. Using two cameras improves the accuracy of measuring the morphology of both coarse and fine particles. It measures the particle size range from 20 µm to 30 mm. Raw data process: the proprietary software is utilised to obtain the size and shape.	Sphericity; convexity	Roundness	-	Particle width	-

Table 8 Descriptions of the morphological indices for the form quantification (summarised from [8, 39, 42, 45, 50, 124-126])

Reference	Description of the morphological indices	Calculation methods
Two-dimensional		
Manual measurement Pentland, 1927 [127]	The Circularity (C) is the ratio of the outline area to circle area. In the equation: A – the outline area; A_C – the longest length as diameter of outline area.	$C = \frac{A}{A_C}$
Manual measurement Tickell, 1931 [124]	The Circularity (C) is the ratio of the outline area to the circumscribed circle. In the equation: A – the outline area; A_C – the area of smallest circumscribed circle.	$C = \frac{A}{A_C}$
Manual measurement Wadell, 1935 [15]	The Sphericity (Ψ) is computed based on the particle and sphere diameters. In the equation: D_A – the diameter of a circle with the same area; D_C – the diameter of the smallest circumscribed circle. The Circularity (C) is the ratio of the circle perimeter to outline perimeter. In the equation: P_C – the circle perimeter with the same area as the particle outline; P – the actual particle outline perimeter.	$\psi = \frac{D_A}{D_C}$

		$C = \frac{P_C}{P}$
Manual measurement Riley, 1941; AIMS Masad et al., 2000; Al-Rousan et al., 2007 [124]	The Circularity (C_1) is expressed as the ratio of the outline area to perimeter, shown in the Equation 1. In the equation: A – the outline area; P – the outline perimeter. The Sphericity (C_2) is expressed as the diameters of inscribed and circumscribed circles, shown in the Equation 2. In the equation: D_I – the diameter of inscribed circle; D_C – the diameter of circumscribed circle. Note: C_1 was reused in 2000 by Masad [8], and in 2007 by Al-Rousan with image analysis [53].	$C_1 = \frac{4\pi A}{P^2}$ (1) $C_2 = \sqrt{\frac{D_I}{D_C}}$ (2)
Fourier series Clark, 1981 [63]	Radius Expansion method is expressed at the right side. In the equations: $r(\theta)$ – the radius length at angle θ; A_n – the phase angles; c_n – the amplitudes. It needs to note that the Equation 1 depends on the point around the periphery from where the outline starts, for that the Equation 2 as the alternative representation is more convenient.	$r(\theta) = a_0 + \sum_{n=1}^{\infty} a_n \sin(n\theta) + \sum_{n=1}^{\infty} b_n \cos(n\theta)$ (1) $r(\theta) = c_0 + \sum_{n=1}^{\infty} c_n \cos(n\theta - A_n)$ (2) $c_n^2 = a_n^2 + b_n^2$ (3) $A_n = \tan^{-1}(b_n / a_n)$ (4)
	Angular bend function is presented at the right side. The outline is presented as chords that change their angular direction. The length and the angle are utilised for the Fourier series. In the equation, $\theta = 2\pi l/L$; L – the total perimeter length; α^* is the cumulative angular change from the origin.	$\alpha^*(l) = c_0 + \sum_{n=1}^{\infty} c_n \cos(n\theta - A_n)$
	In the Complex function, particle outline is treated as a complex function generated by a point moving around the boundary. In the equations, l – the arc length along the outline; $\theta = 2nl/L$; L – the total perimeter length;	$u(l) = x(l) + iy(l)$ (1) $x(l) = \sum_{n=-\infty}^{\infty} c_n \cos(n\theta)$ (2) $y(l) = i \sum_{n=-\infty}^{\infty} c_n \sin(n\theta)$ (3)
PA Janoo, 1998 [54]	The Circularity (C) is computed according to the outline perimeter and area, as shown in the equation. In the equation: P – the perimeter of the particle outline; A – the area of the particle outline. The Feret Diameter was also introduced in [54], which is described as the longitude between two parallel tangents, as shown in Figure a. Based on the Feret Diameter at eight different degrees (0, 22.5, 45, 67.5, 90, 112.5, 135, and 157.5), the convex perimeter is measured as the string around the tips of the eight Ferets (Figure b). Note: as shown in the Figure c & d, the particle area is computed by the sum of pixels within the particle boundary, while the particle perimeter is by the sum of pixels on the particle boundary (figures modified after [54]).	$C = \frac{P^2}{A}$

<table>
<tr>
<td></td>
<td colspan="2">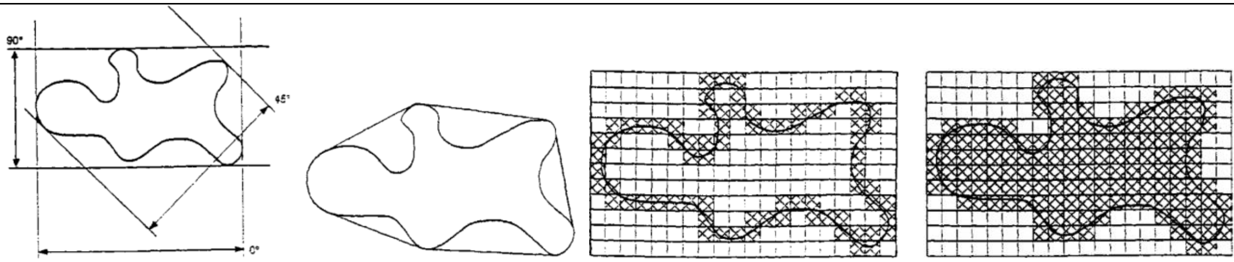

a. Feret Diameter b. Convex perimeter c. Pixels on the particle boundary d. Pixels within the particle boundary</td>
</tr>
<tr>
<td rowspan="2">PA

Brzezicki et al., 1999 [73]</td>
<td>Three dimensions of a particle (L, W, H) are obtained from its shadow, as shown in Figure a & b (figure modified after [73] with permission from ASCE). In the equations: width (W) – BB' (Figure b); height (H) – DD'; length (L) – $A'C'$. Elongated ratio (ER) – the ratio of the length to the width; Flat ratio (FR) – the ratio of the width to the height.</td>
<td>$$ER = L/W \quad (1)$$
$$FR = W/H \quad (2)$$</td>
</tr>
<tr>
<td colspan="2">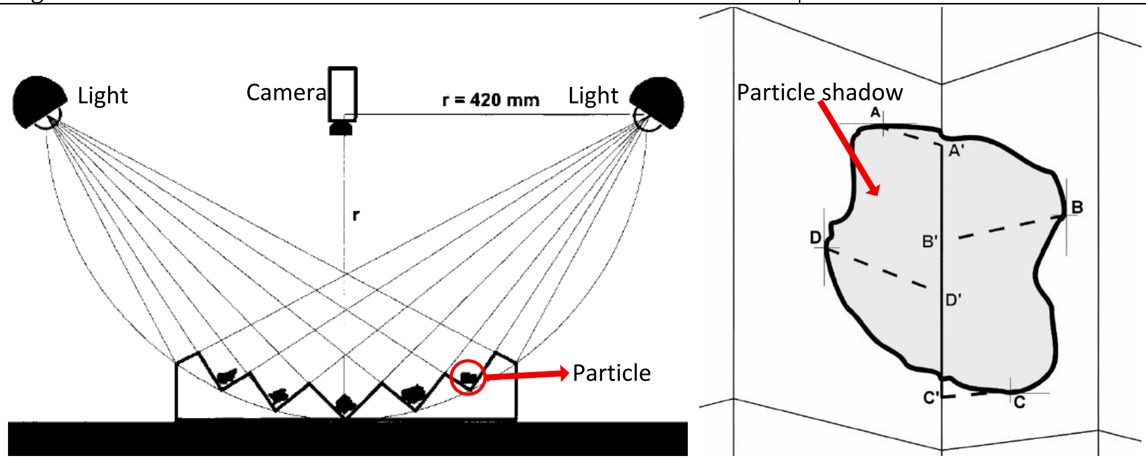

a. Particle shadow acquirement b. Typical outlines of grain shadows</td>
</tr>
<tr>
<td>PA

Mora et al., 2000 [67]</td>
<td>The Convexity ratio (R_C) and the Fullness ratio (R_F) are expressed based on the and the outline area and the convex area, as shown in figure below and the equations at right side (figure modified after [67]). In the equations: Convex area (A_{CON}) – the area of the minimum convex boundaries circumscribing the particle; A – the outline area.</td>
<td>$$R_C = \frac{A}{A_{CON}} \quad (1)$$
$$R_F = \sqrt{\frac{A}{A_{CON}}} \quad (2)$$</td>
</tr>
</table>

	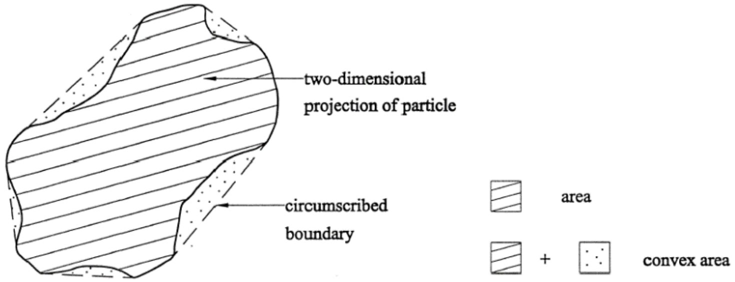 Evaluation of area and convex area	
PA Kuo & Freeman, 2000 [89]	The Form index (FI) is the square of the ratio of the perimeter (P_C) of an equivalent circle to the perimeter (P) of the particle. The Aspect ratio is presented by the ratio of the length to the width. In the equation: Length – the maximum Feret diameter; Width – the minimum Feret diameter. The Feret diameter was introduced at Janoo, 1998 in Table 8.	$$FI = \left(\frac{P_C}{P}\right)^2 \quad (1)$$ $$Aspect\ ratio = \frac{Length}{Width} \quad (2)$$
Fourier series Bowman et al., 2000 [65]	The Fourier descriptor method is to use general shapes to determine the coefficient values of the Fourier shape descriptors. Afterwards the descriptor coefficients of the particle are compared with the descriptor coefficients of the general shapes to decide the particle morphology, as shown in Figure a & b and the equations at right side (figure modified after [65]). In the Equation 1: x, y – coordinates describing the particle outline; N – the total number of descriptors; n – the descriptor number; M – the total number of points describing the particle; m – the index number of a point on the particle; a, b – coefficients for each descriptor; i – an imaginary number. The descriptor coefficient (c_n) is computed by the coefficients for each descriptor (a_n, b_n), as shown in the Equation 2. Note: Fourier shape descriptors (for morphological description): the elongation, trignularity, squareness, irregularity; 0 – Radius, -1 – elongation, -2 – triangularity, -3 – squareness, +l – irregularity, +2 – second order Elongation, +3 – second order triangularity.	$$x_m + iy_m = \sum_{n=-N/2+1}^{N/2} (a_n + ib_n)\left[\cos\left(\frac{2\pi nm}{M}\right) + i\sin\left(\frac{2\pi nm}{M}\right)\right] \quad (1)$$ $$c_n = \sqrt{a_n^2 + b_n^2} \quad (2)$$

<table>
<tr><td></td><td>
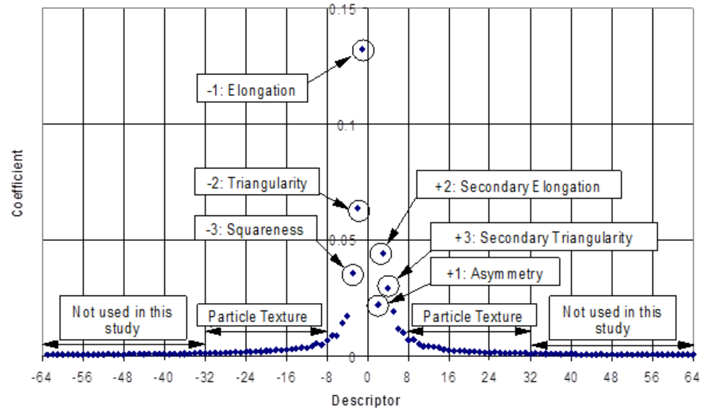

a. Descriptor magnitudes for a typical particle

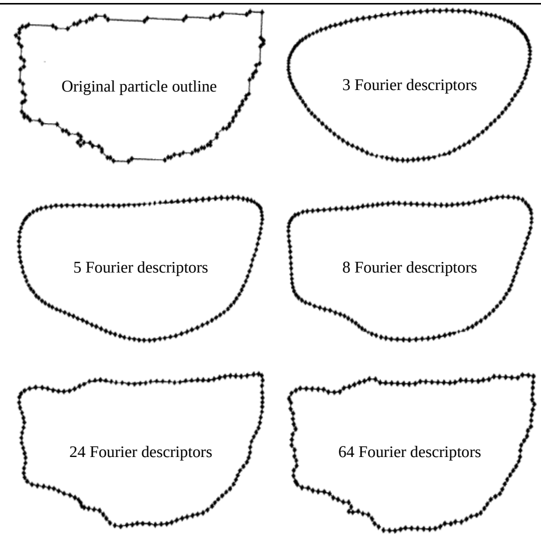

b. The effect of reconstruction of a particle from complex Fourier descriptors using successively fewer descriptors
</td></tr>
<tr><td>PA

Sukumaran & Ashmawy, 2003 [77]</td><td>
The Form index (*FI*) is defined as the deviation of the global particle outline from a circle, as shown in the figure below and the equation at right side (figure modified after [77]). In the equation: N – the number of sampling intervals; α_i – shown in the figure.

$$FI = \frac{\sum_{i=1}^{N} |\alpha_i|}{N \times 45^{\circ}}$$

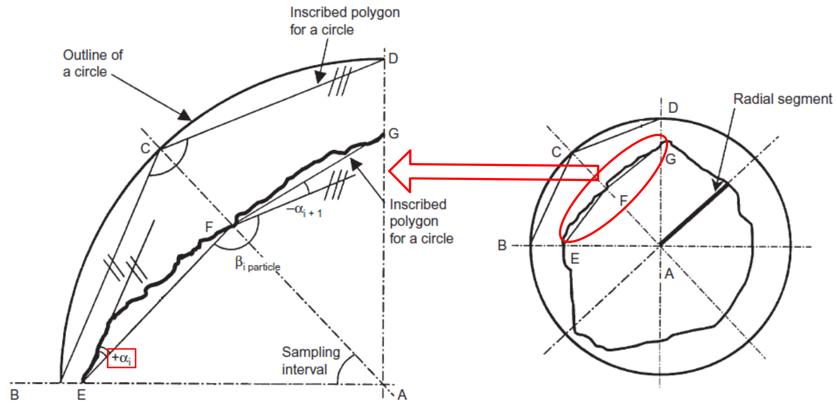

Illustration of the geometric quantities used to determine Slope and Angularity Factors
</td></tr>
</table>

Fourier series Wettimuny et al., 2004 [80]	The Form index (*FI*) is defined as the average of the $TSSR_n$ (n = 2,3,4,5,6), as shown in the Equation 2. The $TSSR_n$ (total summation of the square of residual) is defined as the Equation 1. In the equation: i – the ith sampling angle for the radial measurement; d – the total number of the radial measurements; $r_{o,i}$ – the amplitude of the original radial vector; $r_{o,i\|n}$ – the amplitude of radial vector of the reconstructed shape profile using n largest harmonics.	$TSSR_n = \sqrt{\sum_{i=0}^{d-1}\left(\frac{r_{o,i}-r_{r,i\|n}}{r_{o,i}}\right)^2}$ (1) $FI = \text{average}(TSSR_2, TSSR_3, TSSR_4, TSSR_5, TSSR_6)$ (2)
Fourier series Wang et al., 2005 [81]	The Particle signature parameter α is defined according to the equivalent radius of a circle (R_0) and the average radius (a_0) of the profile outline. In the equation: α_s – the form; α_r – the angularity; α_t – the surface texture; R_0 – obtained with the Equation 2 & 3. In the equation 2 & 3: A – the area of the particle outline. Note: the particle size in this study is around 25 mm in diameter. The following ranges of frequency are used to define the form, angularity, and surface texture should be used, form terms ($m \le 4$); angularity terms ($5 \le m \le 25$); and surface texture terms ($26 \le m \le 180$).	$\alpha = (\frac{R_0}{a_0})^2 = 1 + \frac{1}{2}\sum_{m=1}^{m=n1}[(\frac{a_m}{a_0})^2 + (\frac{b_m}{a_0})^2] + \frac{1}{2}\sum_{m=n1+1}^{m=n2}[(\frac{a_m}{a_0})^2 + (\frac{b_m}{a_0})^2]$ $+ \frac{1}{2}\sum_{m=n2+1}^{m=\infty}[(\frac{a_m}{a_0})^2 + (\frac{b_m}{a_0})^2] = 1 + (\alpha_s + \alpha_r + \alpha_t)$ (1) where $\alpha_s = \frac{1}{2}\sum_{m=1}^{m=n1}[(\frac{a_m}{a_0})^2 + (\frac{b_m}{a_0})^2]$ $\alpha_r = \frac{1}{2}\sum_{m=n1+1}^{m=n2}[(\frac{a_m}{a_0})^2 + (\frac{b_m}{a_0})^2]$ $\alpha_t = \frac{1}{2}\sum_{m=n2+1}^{m=\infty}[(\frac{a_m}{a_0})^2 + (\frac{b_m}{a_0})^2]$ $R_0^2 = A/\pi$ (2) $A = \int_0^{2\pi}\frac{1}{2}R_2(\theta)d\theta = \pi\left[a_0^2 + \frac{1}{2}\sum_{m=1}^{\infty}\left(a_m^2 + b_m^2\right)\right]$ (3)
AIMS Masad et al., 2001; Al-Rousan et al., 2005, 2007 [53]	The Form index (*FI*) is computed by the sum of the incremental changes in the particle radius in all directions. In the equation: R – the radius of the particle in different directions; θ – the directional angle. Note: this morphological index could analyse the 3D images and was utilised by Rousan in 2007.	$FI = \sum_{\theta=0}^{355}\frac{\|R_{\theta+5} - R_\theta\|}{R_\theta}$
Fourier series Sekine et al., 2005 [92]	Aspect ratio with Fourier series (Radius Expansion): $r(\alpha)$ – the distance from the point on the outline to the centre; the nth amplitude spectrum is expressed by the Equation 2; a_n and b_n are expressed by the Equation 3 and 4, respectively; the Aspect ratio is calculated by the ratio of the second and zero order amplitude spectrums, as shown in the Equation 5.	$r(\alpha) = b_0/2 + \sum_{n=1}^{\infty}\{a_n \sin(n\alpha) + b_n \cos(n\alpha)\}$ (1) $c_n = \sqrt{a_n^2 + b_n^2}$ (2) $a_n = \frac{1}{\pi}\int_{\alpha_0}^{\alpha_0+2\pi} r(\alpha)\sin(n\alpha)d\alpha$ n=1,2, (3) $b_n = \frac{1}{\pi}\int_{\alpha_0}^{\alpha_0+2\pi} r(\alpha)\cos(n\alpha)d\alpha$, n=0,1,2 (4)

		$R_{fv} = c_2/c_0$ (5)
Descantes, et al., 2006	The Shape Class Average Ratio (SCAR) is computed by the product of the slenderness ratio and flattening factor. Slenderness ratio (*SR*) is the ratio of the particle length (*a*) to width (*b*), as shown in the equation. The flattening factor is calculated by the ratio of the particle width to an estimate of the average particle thickness	$SR = a/b$
AIMS Al-Rousan et al., 2007 [53]	The Aspect ratio (A_r) is the ratio of the major axe (*L*) to the minor axe (*W*) of the ellipse equivalent to the particle outline. The equivalent ellipse has the same area, first degree moment, and second-degree moment as the particle outline.	$A_r = \frac{L}{W}$
PA Clayton et al., 2009 [128]	The scalene ellipsoid equivalent sphericity (*SEES*) is expressed as the equation at the right side. In the equation: *W* – the mass of the specimen; *n* – the number of particles; G_s – the density; *L* – the average major particle dimension; *I* – the average intermediate particle dimension.	$SEES = \frac{S}{L} = \frac{(W/nG_s)(6/\pi IL)}{L}$
Three-dimensional		
Manual measurement Wentworth, 1922 [49]	The Sphericity (*Ψ*) is expressed based on the three orthogonal dimensions, as shown in the equation at right side. In the equation: *a* – the longest axe; *b* – the medium axe; *c* – the shortest axe.	$\psi = \frac{a+b}{2c}$
Manual measurement Wadell, 1932, 1934 [15]	The Sphericity (Ψ_1) is expressed as the Equation 1. In the equation: S_n – the surface area of a sphere having the same volume as the particle; S_o – the actual surface area. The Sphericity (Ψ_2) is expressed using the particle and sphere volumes, as shown in the Equation 2. In the equation: V_P – the volume of the particle; V_{CIR} – the volume of the circumscribed sphere. The Sphericity (Ψ_3) is expressed using the diameters of the particle and its equivalent sphere, as shown in Equation 3. In the equation: D_{SV} – the sphere diameter with the same volume value as the particle; D_{CIR} – the diameter of a circumscribed sphere.	$\psi_1 = \frac{S_n}{S_o}$ (1) $\psi_2 = \sqrt[3]{\frac{V_P}{V_{CIR}}}$ (2) $\psi_3 = \frac{D_{SV}}{D_{CIR}}$ (3)
Manual measurement Krumbein, 1941 [48]	The Sphericity (*Ψ*) is expressed based on the three dimensions of the particle, as shown in the equation at right side. In the equation: *a* – the longest axe; *b* – the medium axe; *c* – the shortest axe. The chart for determining Sphericity and the Zingg's classification are decided according to the described morphological index, as shown in Figure a & b (figure reproduced from [48]).	$\left(\frac{b}{a}\right)^2 = \frac{\psi^3}{(c/b)}$

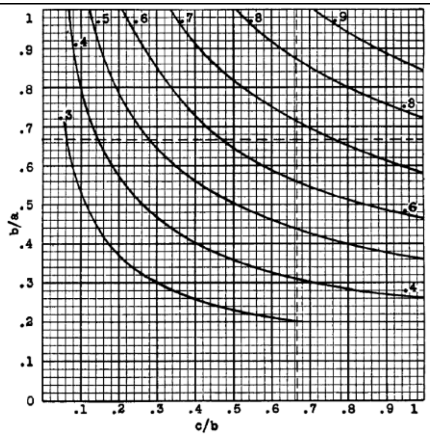

a. Chart for determining sphericity; curves represent lines of equal sphericity

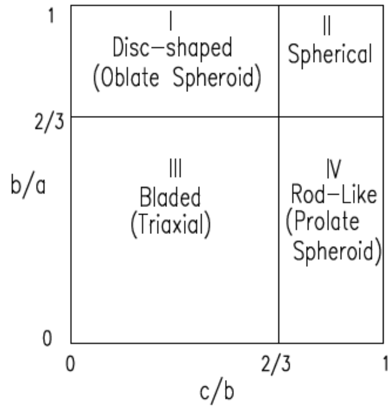

b. Zingg's classification

Manual measurement Pye & Pye, 1943; Kuo et al., 1996 [89]	The Sphericity (Ψ) is expressed based on the three dimensions of the particle, as shown in the equation at right side. In the equation: *a* – the longest axe; *b* – the medium axe; *c* – the shortest axe. Note: this morphological index was also used by Kuo in 1996 with image analysis.	$\psi = \sqrt[3]{\frac{b \cdot c}{a^2}}$
Manual measurement Corey, 1949; PA Barksdale et al., 1991; Kuo et al., 1996 [64]	The Form index (*FI*) is expressed based on the three dimensions of the particle, as shown in the equation at right side. In the equation: *a* – the longest axe; *b* – the medium axe; *c* – the shortest axe. Note: this parameter was used by Barksdale in 1991, and also by Kuo in 1996.	$FI = \frac{c}{\sqrt{a \cdot b}}$
Manual measurement Aschenbrenner, 1956 [129]	The Form index (*FI*) is expressed based on the three dimensions of the particle, as shown in the equation at right side. In the equation: *a* – the longest axe; *b* – the medium axe; *c* – the shortest axe.	$FI = \frac{a \cdot c}{b^2}$
Manual measurement Williams, 1965 [130]	The Form index (*FI*) is expressed based on the three dimensions of the particle, as shown in the equations at right side. In the equation: *a* – the longest axe; *b* – the medium axe; *c*– the shortest axe.	$FI = 1 - \frac{a \cdot c}{b^2}$ when $b^2 > ac$; $FI = \frac{a \cdot c}{b^2} - 1$ when $b^2 \le ac$
Manual measurement Janke, 1966 [124]	The Form index (*FI*) is expressed based on the three dimensions of the particle, as shown in the equation at right side. In the equation: *a* – the longest axe; *b* – the medium axe; *c*– the shortest axe.	$FI = \frac{c}{\sqrt{\frac{a^2 + b^2 + c^2}{3}}}$

Manual measurement Dobkins & Folk, 1970 [131]	The Oblate-prolate index (*OPI*) is expressed based on the three dimensions of the particle, as shown in the equation at right side. In the equation: *a* – the longest axe; *b* – the medium axe; *c* – the shortest axe.	$OPI = \dfrac{10\left(\dfrac{a-b}{a-c}-0.5\right)}{\dfrac{c}{a}}$
Manual measurement Sneed & Folk, 1985 [47]	The Sphericity (*Ψ*) is expressed based on the three dimensions of the particle, as shown in the equation at right side. In the equation: *a* – the longest axe; *b* – the medium axe; *c* – the shortest axe.	$\psi = \sqrt[3]{\dfrac{c^2}{a \cdot b}}$
PA Kuo et al., 1996 [89]	The Sphericity (*Ψ*) is expressed based on the three dimensions of the particle, as shown in the Equation 1. In the equation: *a* – the longest axe; *b* – the medium axe; *c* – the shortest axe. The Form index (*FI*) is expressed based on the three dimensions of the particle, as shown in the Equation 2. In the equation: *a* – the longest axe; *b* – the medium axe; *c* – the shortest axe. Note: the above-mentioned two morphological indices were proposed by Krumbein in 1941 [48] and Corey in 1949 [124], respectively, with manual measurement. Afterwards, Kuo utilised them with image analysis method. The method acquires the two perpendicular projections of one particle for 3D analysis.	$\psi = \sqrt[3]{\dfrac{b \cdot c}{a^2}}$ (1) $FI = \dfrac{c}{\sqrt{a \cdot b}}$ (2)
Fourier series Lanaro, 2001 [75]	The Fourier series is utilised for the form estimation by comparing the power spectrum of particle image cross-section with that of the particle shape categories, shown in Figure a (modified after [75]). The power spectrum is expressed based on the equations at right side. Equation 1 is the Fourier transform. In the equation, the *u/M* and *v/n* are the frequency variables, and the sine and cosine curves explicitly appear when using Euler's formula for *i*. Equation 2 is the theoretical expression of the power spectrum (Figure b). In the equation: *1/X* – the period of the frequency spectrum; *AX* – the maximum value of the spectrum.	$F(u,v) = F\{f(x,y)\} = \sum_{u=0}^{M-1}\sum_{v=0}^{N-1} f(x,y) \cdot \exp\left[-2\pi i\left(\dfrac{xu}{M}+\dfrac{yv}{N}\right)\right]$ (1) $\lvert F(u)\rvert = AX\left\lvert\dfrac{\sin(\pi uX)}{\pi uX}\right\rvert$ (2)

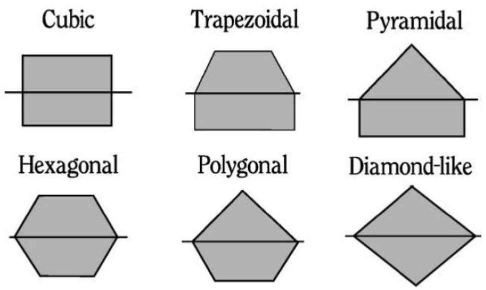

a. Particle shape categories

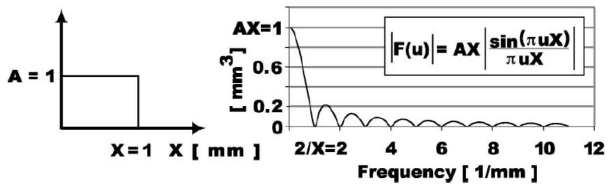

b. Frequency spectrum for a rectangular

LASS Kim et al., 2002 [51]	The Form index (*FI*) is expressed as the Equation 1. In the equation: *E* – energy, summation of absolute values of all the elements; $d_{i,j,k,l}$ – wavelet coefficients at a decomposition level *i*. The wavelet coefficients ($d_{i,j,k,l}$) are obtained from two steps. Equation 2 is the first step, which is to transform Cartesian coordinates into the polar coordinates. In the equation: α – the horizontal angle; β – the vertical angle; *i* – the decomposition level; *j* – the scale coefficients; *k* – the translation coefficients; $f(\alpha, \beta)$ – the length of the radius vector at angle α and β; $W_{i,j,k,0} = \varphi(2^{-i}\alpha^{-j})\psi(2^{-i}\beta^{-k})$; $W_{i,j,k,1} = \psi(2^{-i}\alpha^{-j})\varphi(2^{-i}\beta^{-k})$; $W_{i,j,k,2} = \psi(2^{-i}\alpha^{-j})\psi(2^{-i}\beta^{-k})$. Equation 3 is the second step, which is to express the Wavelet coefficients. Note: the detailed procedures of wavelet transform decomposing for signals are introduced in [51].	$FI = \frac{E\left(d_{0,j,k,l}\right)+E\left(d_{1,j,k,l}\right)}{\text{average radius}}$ (1) $d_{i,j,k,l} = \left[f(\alpha,\beta), W_{i,j,k,l}(\alpha,\beta)\right] = \int^{\infty} f(\alpha,\beta)W_{i,j,k,l}(\alpha,\beta)d\alpha d\beta \quad i,j,k \in Z, l \in [0,2]$ (2) $f(\alpha,\beta) = \sum_{i=-\infty}^{\infty}\sum_{j=-\infty}^{\infty}\sum_{k=-\infty}^{\infty}\sum_{l=0}^{2} d_{i,j,k,l}W_{i,j,k,l}(\alpha,\beta) \quad i,j,k \in Z, l \in [0,2]$ (3)
Fourier series Garboczi et al., 2002 [82]	The first step is to measure the radius of the particle at 240 surface points, which are Gaussian quadratures. Afterwards, the Equation 1 is utilised to reconstruct the particle. In the Equation 1: $R(\theta, \phi)$ – the radius measured from the centroid to the surface; θ – the angle measured from positive z-axe ($0, \pi$); ϕ – angle measured from positive x-axe ($0, 2\pi$); *n* – degree; *m* – order; $Y_n^m(\theta,\phi)$ – the spherical harmonic function at degree *n* and order *m* (expressed in the Equation 2). The quantification of particle form, angularity and surface texture is according to solving the a_{nm} in the Equation 3. The asterisk denotes the complex conjugate in Equation 3. The functions $P_n^m(x)$ are the associated Legendre function and are a set of orthogonal polynomials found in quantum mechanics (more descriptions in [82]).	$R(\theta,\phi) = \sum_{n=0}^{\infty}\sum_{m=-n}^{n} a_{nm}Y_n^m(\theta,\phi)$ (1) $Y_n^m(\theta,\phi) = \sqrt{\left(\frac{(2n+1)(n-m)!}{4\pi(n+m)!}\right)}P_n^m(\cos(\theta))e^{im\phi}$ (2) $a_{nm} = \int_0^{2\pi}\int_0^{\pi} d\phi d\theta \sin(\theta) R(\theta,\phi) Y_n^{m*}$ (3)
AIMS Fletcher et al., 2003; Chandan et al., 2004; Al-Rousan et al., 2007 [53]	The Sphericity (Ψ) is expressed with the ratios of the dimensions of the particle. In the equation: *a* – the longest axe; *b* – the medium axe; *c* – the shortest axe. The Form index (*FI*) is expressed by the ratios of the dimensions of the particle. Note: the methods for the dimension acquisition applied in AIMS are introduced briefly as follow. The three dimensions are measured using the autofocus microscope (for the shortest axe) and the grey images (for the longest and the medium axes). For the grey images, the eigenvector method is utilised for the longest and medium axes of a 2D particle outline. Each pixel in the particle outline is treated as a 2D vector. The vectors are utilised for the calculation of the mean vector and covariance matrix. Afterwards, the covariance matrix eigenvectors that are orthogonal to each other are analysed. The major and minor axes of the outline are aligned along the orthogonal eigenvectors. The length of the axes is the same as the distance from the particle centroid to the outline along the two orthogonal eigenvectors.	$\psi = \sqrt[3]{\frac{d_s \cdot d_I}{d_L^2}}$ (1) $FI = \frac{d_s}{d_L \cdot d_I}$ (2)
Fourier series Masad et al., 2005 [8]	Based on the theory of Spherical harmonic series, proposed by Garboczi et al. in 2002, the three descriptors are decided respectively for the form, angularity or surface texture. As shown in the equations at right side, the Form index (*FI*) was taken as the summation of indices with $1 < n < 4$; the Angularity	$FI = \sum_{n=0}^{5}\sum_{m=-1}^{n}\left\|a_{nm}\right\|$ (1)

	index (*AI*) is quantified with $5 < n < 25$; the Surface texture index (*STI*) is quantified with $n \leq 25$.	$$AI = \sum_{n=6}^{25} \sum_{m=-1}^{n} \lvert a_{nm} \rvert \quad (2)$$ $$STI = \sum_{n=26}^{n\max} \sum_{m=-1}^{n} \lvert a_{nm} \rvert \quad (3)$$
3D image analysis Hayakawa et al., 2005 [59]	The Modified Wadell's Sphericity (E_s) is proposed to express the similarity of a particle to an ellipsoid with the same dimensions. In the equation: e_n – the surface area of an ellipsoid with the same dimensions, expressed as the Equation 2; S – the surface area of the particle.	$$E_s = e_n / S \quad (1)$$ $$e_n = \frac{\pi}{2}\left(c^2 + b\sqrt{a^2-c^2}\int_0^{\alpha}\sqrt{1-k^2\sin^2\varphi}\,d\varphi + \frac{bc^2}{\sqrt{a^2-c^2}}\int_0^{\alpha}\frac{d\varphi}{\sqrt{1-k^2\sin^2\varphi}}\right) \quad (2)$$
3D image analysis Fernlund, 2005, 2007 [9]	The Elongated or Flat ratio (*ER* or *FR*) are expressed as the equations at right side. In the equation: *a* – the longest axe; *b* – the medium axe; *c* – the shortest axe. In [9], the authors used two particle images (in lying and standing positions) for the three dimensions acquisition.	$$ER = \frac{a}{b} \quad (1)$$ $$FR = \frac{b}{c} \quad (2)$$
3D image analysis Erdoğan et al., 2006 [76]; Anochie-Boateng et al., 2012, 2013 [46]	Compared with the last method, the Elongated or Flat ratio (*ER* or *FR*) are expressed with the same equations, shown at right side. In the equation: *a* – the longest axe; *b* – the medium axe; *c* – the shortest axe. Additionally, the difference is the means of image acquisition. Specifically, Anochie-Boateng utilised 3D images from laser scanning for individual ballast particle analysis, while Erdoğan used those from the X-ray computed tomography.	$$ER = \frac{a}{b} \quad (1)$$ $$FR = \frac{b}{c} \quad (2)$$
UIAIA Tutumluer et al., 2005 [42]	The Flat & Elongated ratio (*FE*) is expressed with the longest dimension and the shortest perpendicular dimension, as shown in the equation at right side.	$$FE = \frac{Longest\ Dimension}{Shortest\ Perpendicular\ Dimension}$$
PA Le Pen et al., 2013 [83]	The Ellipseness (*E*) is expressed as the equation at right side. In the equation: P_e – the perimeter of an ellipse having the same area as the particle outline; P_o – the actual perimeter of the outline. The ellipse has the same major dimension and area as the particle outline.	$$E = \frac{P_e}{P_o}$$
3D image analysis Sun et al., 2014 [50]	The Ellipsoidness (*E*) is expressed as the ratio of the surface area (S_e) of the equivalent ellipsoid to the particle surface area (S_o), as shown in the Equation 3. In the equation: *a* – one half of the longest axe; *b*, *c* – the minor radius, obtained from Equation 1 ($b = c$); *V* – particle volume; S_e – obtained with the Equation 2.	$$b = \left(\frac{3V}{2\pi L}\right)^{1/2} \quad (1)$$ $$S_e = 4\pi\left(b^2 + a^2\frac{\cos^{-1}(b/a)}{\tan[\cos^{-1}(b/a)]}\right) \quad (2)$$ $$E = S_e / S_o \quad (3)$$

3D image analysis Ouhbi et al., 2017 [132]	The Form index (*FI*) is expressed based on the difference between each grain and the average grain. The radius differences written in Equation 2 define matrix *A*, and its line vectors Δr_i for $1 \le i \le n$, by subtracting vector r from each line of A_1. For any matrix *a* denote its Frobenius norm as $\lVert a \rVert$: $\lVert a \rVert^2 = \sum_i \sum_j a_{ij}^2$. $\lVert \overline{r} \rVert$ being the norm of *d*-dimensional vector $\overline{r}$, one has the definition as Equation 3. The importance of the variation from grain to grain, relatively to the average shape, is expressed as the Equation 4.	$\overline{r}_j = \frac{1}{n}\sum_{k=1}^{n} r_{kj} (1 \le j \le d)$ (1) $\Delta r_{ij} = r_{ij} - \overline{r}_j$ (2) $\lVert A_1 \rVert^2 = n \lVert \overline{r} \rVert^2 + \lVert A \rVert^2$ (3) $\delta_1 = \frac{\lVert A \rVert}{n^{1/2} \lVert \overline{r} \rVert}$ (4)

Table 9 Morphological indices for the angularity quantification (summarised from [8, 39, 42, 45, 50, 124-126])

Reference	Description of the morphological indices	Calculation methods
Manual measurement Wentworth, 1923 [49]	Wentworth proposed four methods for Roundness quantification (R_1, R_2, R_3, R_4): In the Equation 1: *L* – the longest axe of the maximum particle projection; S_M – the shortest axe of the minimum projection; D_s –the diameter of a circle fitting the sharpest corner. In the Equation 2: *L* – the longest axe; *B* – the intermediate axe, perpendicular to the longest axe; R_{CON} – the radius of the most convex part. In the Equation 3: D_S – the diameter of the sharpest corner; D_X – the diameter of a pebble trough the sharpest corner. In the Equation 4: R_{CON} – the radius of the sharpest corner; R_{AVG} – the average radius of the pebble, calculated with the Equation 5.	$R_1 = \frac{D_S}{(L + S_M)/2}$ (1) $R_2 = \frac{R_{CON}}{(L + B)/4}$ (2) $R_3 = \frac{D_S}{D_X}$ (3) $R_4 = \frac{R_{CON}}{R_{AVG}}$ (4) $R_{AVG} = \frac{1}{2} D_{AVG} = \frac{1}{2}\sqrt[3]{a*b*c}$ (5)
Manual measurement Szadeczsky-Kardos, 1933 [124]	The Roundness (*R*) is expressed as the equation at right side. In the equation: P_{CON} – the perimeter of concave parts; *P* – the perimeter of the particle outline.	$R = \frac{P_{CON}}{P} * 100$

Manual measurement Fischer, 1933 [124]	The particle central point joins the outline points to divide the outline into the non-curved parts and the convex parts. Based on that, two equations are used to express the Roundness (R_1, R_2), as shown at right side. In the equations: ANG_{PLA} – the central angles of the non-curved parts; ANG_{CON} – the central angles of the convex parts.	$R_1 = \frac{\sum ANG_{PLA}}{360°}$ (1) $R_2 = \frac{\sum ANG_{CON}}{\sum ANG_{PLA}}$ (2)
Manual measurement Wadell, 1935	The Roundness (R) is expressed with the average radius of the corners and the inscribed circle diameter, as shown in the equation at right side. In the equation: $R_{max\text{-}in}$ – the radius of the inscribed circle; r – the radius of the corners. Note: many studies made a chart (classification) based on this morphological index for comparison [16, 48, 133].	$R = \frac{\sum \left(\frac{r}{R_{\text{max-in}}} \right)}{N}$
Manual measurement Cailleux, 1947 [124]	The Roundness (R) is expressed with the radius of the most convex part and the longest axe, as shown at right side. In the equation: R_{CON} – the radius of the most convex part of the particle outline; L – the longest axe of the particle outline.	$R = \frac{R_{CON}}{L/2}$
Manual measurement Kuenen, 1956 [134]	The Roundness (R) is expressed as the equation. In the equation: D_S – the diameter of circle fitting sharpest corner; B – the intermediate axe of the particle outline.	$R = \frac{D_S}{B}$
Manual measurement Lees, 1964	The Roundness (R) is expressed by measuring the angularity instead of the roundness, as shown in figure below and the equation at right side (figure modified after [55]). In the equation: α – the angles; $R_{max\text{-}in}$ – the radius of the largest inscribed circle of the particle outline; x – the distance of the tip of the corner from the centre of the largest inscribed circle.	$R = (180 - \alpha) \frac{x}{R_{\text{max-in}}}$

[55]	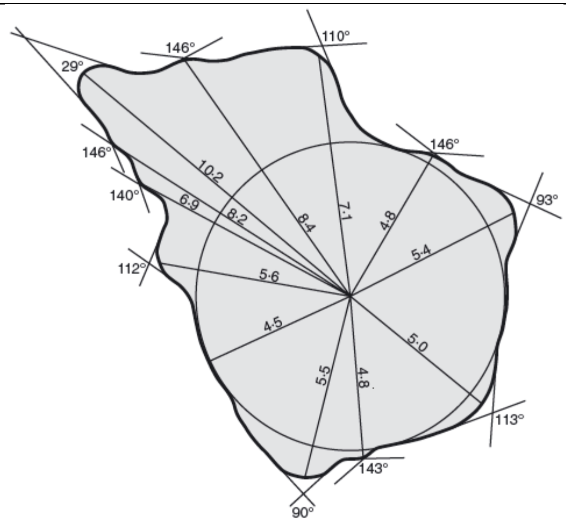	
Manual measurement Dobkins & Folk, 1970 [131]	The Roundness (R) is expressed with the sharpest corner and inscribed circle diameters, as shown in the equation at right side. In the equation: D_S – the diameter of circle fitting sharpest corner; D_i – the diameter of the largest inscribed circle of the particle outline.	$R = \frac{D_S}{D_i}$
Manual measurement Swan, 1974 [135],	The Roundness (R) is expressed with the sharpest corner and inscribed circle diameters, as shown in the equation at right side. In the equation: D_{S1}, D_{S2} – the diameter of circle fitting sharpest corner and the second sharpest corner, respectively; D_i – the diameter of the largest inscribed circle of the particle outline.	$R = \frac{(D_{S1} + D_{S2})/2}{D_i}$
PA Palasamudram & Bahadur, 1997 [62]	The Angularity index (A_n) is expressed as the Equation 1. In the equation: K – an arbitrary constant; i – the ith angle of the particle outline; a_i – expressed as the Equation 2; α_i – the ith angle degree; p_i – expressed as the Equation 3.	$A_n = K\sum_{i=1}^{n} a_i \cdot p_i$ (1) $a_i = K/\alpha_i$ (2) $p_i = \frac{\pi - \alpha_i}{2\pi}$ (3)
PA Janoo, 1998;	The Roundness (R) is expressed with the particle outline perimeter and the particle outline area, as shown in the equation at right side. In the equation: P – the particle outline perimeter; A – the particle outline area.	$R = \frac{4\pi A}{P^2}$

Kuo & Freeman, 1998, 2000 [54]		
PA Sukumaran & Ashmawy, 2001, 2003 [77]	The Angularity index (AI) is expressed as the equation. In the equation: N – the number of sampling intervals; $\beta_{iparticle}$ – angle EFG in the figure (Sukumaran & Ashmawy, 2001, 2003) in Table 8.	$AI = \frac{\sum_{i=1}^{N}(\beta_{i\ \text{particle}}-180)^2-(360^2/N)}{3\times(180)^2-(360^2/N)}\times 100\%$
AIMS Masad et al., 2001 [8]	The Angularity index (AI) is expressed with the distance difference in a certain direction between the distance from the inscribed circle centre to the corner and the equivalent ellipse radius, as shown in the equation at right side. In the equation: R_θ – the distance from the inscribed circle centre to the corner at the directional angle θ; $R_{EE\theta}$ – the radius of the equivalent ellipse at the same directional angle θ.	$AI = \sum_{\theta=0}^{\theta=360-\Delta\theta}\frac{\lvert R_\theta - R_{EE\theta}\rvert}{R_{EE\theta}}$
AIMS Masad et al., 2000 [53]	The Angularity index (SP) is expressed as the equation at right side. It is obtained with the surface Erosion-Dilation technique as shown in the figure below (figure reproduced from [53]). In the equation, A_1 and A_2 are the areas of particle image before and after applying the Erosion-Dilation operations, respectively. Note: more angular particles lose more area when applying the Erosion-Dilation operations. Additionally, the SP could be used to analyse the angularity in low resolution images, while the higher resolution images can be utilised for surface texture analysis.	$SP = \frac{A_1 - A_2}{A_1}\times 100\%$
	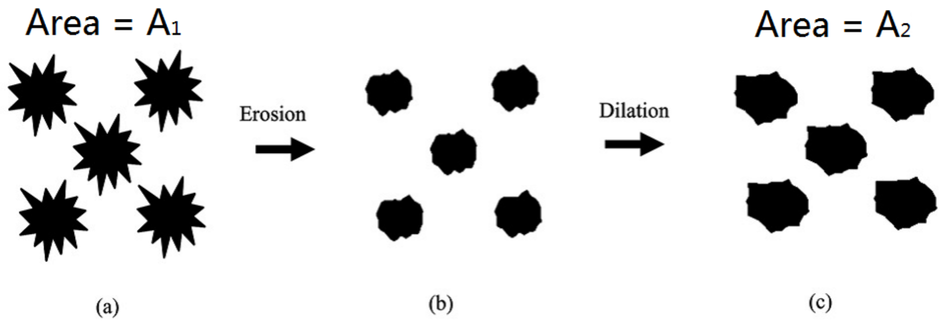 Erosion-Dilation Technique	
LASS Kim et al., 2002 [51]	The Angularity index (AI) is expressed as the equation at right side. The explanations of the equation are at the part of Wavelet transform (LASS; Kim et al., 2002) in Table 8.	$AI = \frac{E\left(d_{2,j,k,l}\right)+E\left(d_{3,j,k,l}\right)}{\text{average radius}}$

Fourier series Wang et al., 2005 [81]	The Angularity index (α_r) is expressed as the equation at right side. The details of the equation were explained at the Fourier series (Wang et al., 2005) in Table 8.	$\alpha_r = \sum_{j=5}^{25}\left[\left(\frac{a_n}{a_0}\right)^2 + \left(\frac{b_n}{a_0}\right)^2\right]$
3D image analysis Hayakawa et al., 2005 [59]	The Roundness (X_s) is expressed as the equation at right side. In the equation: *a* – the longest axe; *b* – the medium axe; *c* – the shortest axe; *V* – particle volume; *S* – particle surface area.	$X_S = V/S(abc)^{1/3}$
AIMS Chandan et al., 2004; Al-Rousan et al., 2005 [53]	The Angularity index (*AI*) is expressed based on the change in the gradient on a particle outline, named the gradient method. In the equation: *i* – the *i*th point on the particle outline; *N* – total number of points on the particle outline; θ_i – the angle of orientation values of the *i*th edge points.	$AI = \frac{1}{N/3-1}\sum_{i=1}^{N-3}\left\|\theta_i - \theta_{i+3}\right\|$
UIAIA Tutumluer et al., 2005 [42]	The Angularity index (*AI*) is computed by averaging the Angularity index values of three orthogonal views (weighted by their areas) as the Equation 1 & 2. In the equations: *e* – the starting angle value for each 10° class interval (0, 10, 20, 30,…,170), as shown in the Figure b, the horizontal axis; *P(e)* – the probability that the angle change β in the range of *e* to *(e + 10)*. β is expressed as the Equation 3. In the equation: α_n – the subtended angle at the *n*th vertex, as shown in the Figure a. (figure reproduced from [53])	$AI = \frac{A(\text{front})\times \text{Area(front)} + A(\text{top})\times \text{Area(top)} + A(\text{side})\times \text{Area(side)}}{\text{Area(front)} + \text{Area(top)} + \text{Area(side)}}$ (1) $A = \sum_{e=0}^{170} e \times P(e)$ (2) $\beta_n = (\alpha_n - \alpha_{n-1})$ (3)
	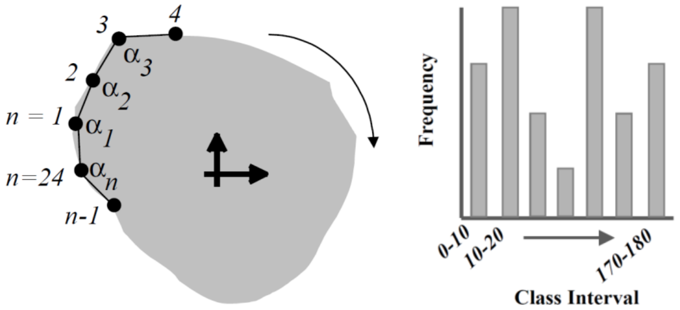 a. Illustration of An n-sided Polygon Approximating the Outline of a Particle b. Frequency distribution for the change in vertex angles	
Fourier series Sekine et al., 2005 [92]	Angularity index is calculated with the Fourier series (Argument function). The Argument function applies the distance of the outline point and the reference point, as well as the angle between the tangential line (outline point) and the reference line (reference point). In the equations: *L* – the outline perimeter; $\theta_N(x)$ is a periodic function with the period *L*; the Angularity index (*AI*) is calculated by the sum of the third to	$\theta(x+L) = \theta(x) + 2\pi$ (1) $\theta_N(x) = \theta(x) - 2\pi(x/L)$ (2)

	twentieth amplitude spectra, as presented in the Equation 7.	$$\theta_N(x) = b_0/2 + \sum_{n=1}^{\infty}\{a_n \sin(2\pi nx/L) + b_n \cos(2\pi nx/L)\} \quad (3)$$ $$c_n = \sqrt{a_n^2 + b_n^2} \quad (4)$$ $$a_n = \frac{2}{L}\int_{x_0}^{x_0+L} f(x)\sin(2\pi nx/L)dx \text{, n=1,2,…..} \quad (5)$$ $$b_n = \frac{2}{L}\int_{x_0}^{x_0+L} f(x)\cos(2\pi nx/L)dx \text{, n=0,1,2…} \quad (6)$$ $$AI = \sum_{k=3}^{20} c_k \quad (7)$$
Descantes et al., 2006	The Angularity index (*AI*) is calculated by measuring the average value of the sharpest salient angles between two adjacent straight lines (Figure). In the equation: α_i – salient angle between two adjacent straight lines; n – number of angles that are taken into consideration ($n \leq 8$).	$$AI = \frac{1}{n}\sum_{i=1}^{n}(1 - \frac{\alpha_i}{180})\alpha_i \in [0,180^\circ]$$
PA Zhang et al., 2012 [71]	The AT index (*AT*) is a morphological index to characterise the combination of the angularity and the surface texture. The AT index of an aggregate particle is computed by averaging the AT_i values of the particle's different cross sections, and they are weighted by their areas, as shown in equations at right side. In the Equation 2: P_O – the outline perimeter of the ith cross section; P_C – the perimeter of the convex outline of the ith cross section. In the equation 1: A_i – the area of the ith cross section.	$$AT = \frac{\sum_1^n A_i \cdot AT_i}{\sum_1^n A_i} \quad (1)$$ $$AT_i = \frac{P_O - P_C}{P_C} \quad (2)$$
	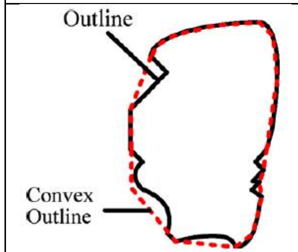	

Table 10 Morphological indices for the surface texture quantification (summarised from [8, 39, 42, 45, 50, 124-126])

Reference	Description of the morphological indices	Calculation methods

Manual measurement Wenzel, 1949 [56]	The Roughness factor (*R*) is expressed as the equation at right side. In the equation: *A* – the surface area of the particle; *a* – the surface area of the particle outline.	$R = \frac{A}{a}$
Barksdale et al., 1991 [64]	The Roughness factor (*R*) is expressed as the equation at right side. In the equation: L_T – true length of the surface segment being analysed; L_P – length of the line of best fit for the surface segment.	$R = L_T / L_P$
PA Hyslip et al., 1997 [66]	The quantitative descriptor of roughness (D_R) is computed by solving it from the Equation 1. As shown in the figure below, the particle outline is divided into segments for roughness quantification (figure modified after [66]). In the Equation 1: $P(\lambda)$ – the length of the line (curve) based on unit measurement length λ; *n* – a proportionality constant (equal to the actual and indeterminate length of the line). By taking the logarithm of both sides of Equation 1, the roughness descriptor (D_R) is related to the linear slope coefficient, *m*, as shown in Equation 2. In the Equation 2: *m* – the linear slope coefficient.	$P(\lambda) = n\lambda^{1-D_R}$ (1) $D_R = 1 - m$ (2)
	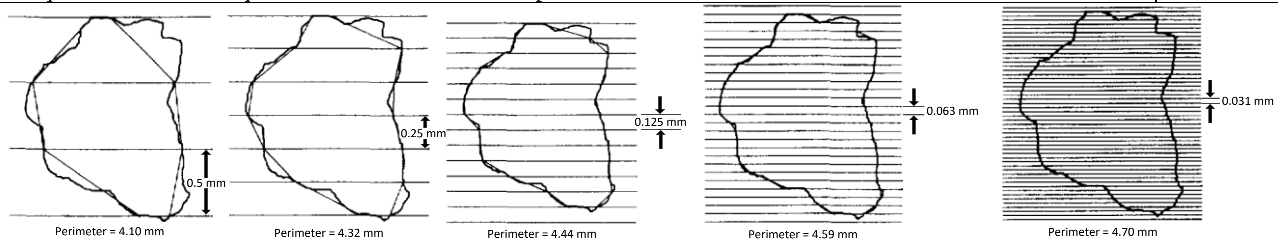	
PA Janoo, 1998[54]	The Roughness (*R*) is expressed as the equation at right side. In the equation: *P* – the perimeter of the particle outline; C_{PER} – the convex perimeter of the particle outline. Note: the convex is explained with the figure shown at Janoo, 1998 in Table 8.	$R = \frac{P}{C_{PER}}$
PA Kuo et al., 1998 [89]	The Roughness (*R*) is expressed as the equation at right side. In the equation: *P* – the perimeter of the particle outline; D_{AVG} – the average of the 12 Feret diameters (details explained at Janoo, 1998 in Table 8).	$R = \frac{P}{\pi * D_{AVG}}$
Fourier series Bowman et al., 2000 [65]	The Fourier shape descriptors (c_n) uses higher order descriptors to present the particle surface texture. The computation method was introduced at Bowman et al., 2000, in Table 8. It is proposed that the descriptors from +/-8 to +/-32 can measure of the particle surface texture.	-
AIMS Masad et al., 2000 [53]	The Surface texture index (*SP*) is expressed as the equation at right side. In the equation: A_1 and A_2 are the areas of particle image before and after applying the Erosion-Dilation operations, respectively. The Erosion-Dilation technique was explained in the former part (angularity) at Masad, 2000 in Table 9. Note: the equation used for surface texture quantification is the same one used for the angularity quantification. Because the *SP* can quantify both surface texture and angularity after controlling the image resolution. The high-resolution image can cause the fine details (surface texture) disappear, and for that it can be used for the surface texture quantification.	$SP = \frac{A_1 - A_2}{A_1} \times 100\%$
Fourier series Lanaro et al., 2001	Fractal surfaces are dependent on the frequency ranges following a power law of the spatial frequency for an isotropic surface with fractal constant F_0 given by Equation 1. The Hurst exponent H correlates with the Fractal dimension (*FR*) as explained at Hyslip et al., 1997 (Equation 2). The roughness is characterised by the *FR* or *H* and the F_0.	$\lvert F(u,v) \rvert = F_0(\sqrt{u^2 + v^2})^{-\alpha/2}$

		(1) $FR = 3 - H = (7-\alpha)/2$ (2)
LASS Kim et al., 2002 [51]	The Surface texture index (*STI*) is expressed as the equation at right side. The explanations of the variables in this equation are at the Wavelet transform in Table 8 (Kim et al., 2002).	$STI = \frac{E\left(d_{4,j,k,l}\right) + E\left(d_{5,j,k,l}\right)}{\text{average radius}}$
AIMS Fletcher et al., 2002-2003; Chandan et al., 2004 [53]	The Surface texture index (STI_n) is expressed as the equation. In the equation: *n* – the decomposition level; *N* – the total number of coefficients in a detailed image of texture; *i* – taking the values 1, 2, or 3, for the three detailed images of texture; *j* – the wavelet coefficient index; (x, y) – the location of the coefficients in the transformed domain. Note: The Wavelet transform was briefly introduced at the LASS in Table 8 (Kim et al., 2002). The decomposition level, $n = 6$, are utilised, because level 6 is the least affected by colour discrepancies and the dust existence on the surface.	$STI_n = \frac{1}{3N}\sum_{i=1}^{3}\sum_{j=1}^{N}[D_{ij}(x,y)]^2$
Fourier series Wettimuny et al., 2004 [80]	The Roughness factor (*RF*) is expressed as the equation at right side. In the equation: $TSSR_1$ – defined by the equation of $TSSR_n$ when the $i = 1$ (details explained at Wettimuny et al., 2004 in Table 8); *FI* – the average of the $TSSR_n$ (n = 2,3,4,5,6).	$RF = TSSR_1 - FI$
Fourier series Wang et al., 2005 [81]	The Surface texture index (α_t) is expressed as the equation at right side. The details of the equation were explained at the Fourier series (Wang et al., 2005) in Table 8.	$\alpha_t = \sum_{j=26}^{180}\left[(\frac{a_n}{a_0})^2 + (\frac{b_n}{b_0})^2\right]$
UIAIA Tutumluer et al., 2005	The Surface texture index (*ST*) is expressed as the Equation 1. In the equation: A_1 – area of the particle outline before Erosion-Dilation operation; A_2 – area of the particle outline after n cycles of Erosion-Dilation operation. The Erosion-Dilation cycles (*n*) is determined by the Equation 2. In the equation: *L* – longest intercept of a particle outline; β – scaling factor for erosion and dilation operations (constant value). The final particle surface texture ($ST_{particle}$) is computed as the weighted average of each *ST* value form three orthogonal views, shown in Equation 3. In the equation: *i* – from 1 to 3 for top, front, and side views.	$ST = \frac{A_1 - A_2}{A_1} \times 100$ (1) $n = \frac{L}{\beta}$ (2) $ST_{particle} = \frac{\sum_{i=1}^{3} ST(i) * Area(i)}{\sum_{i=1}^{3} Area(i)}$ (3)
Descantes et al., 2006	The roughness (*STI*) is calculated with the length of a straight line segment (L_{perim}) and the corresponding outline length (L_{seg}), as shown in the figure below (reproduced from [122]).	$STI = mean(\frac{L_{perm} - L_{seg}}{L_{perm}})$

	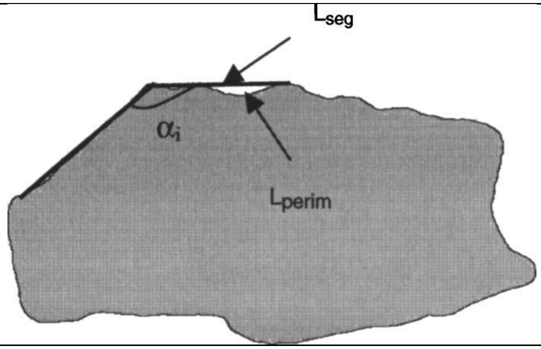	

Table 11 Calculation methods with the Image analysis for particle size evaluation

Reference	Description of the morphological indices	Calculation methods
Hyslip & Vallejo, 1997	Fragmentation fractal dimensioning (D_F) is proposed for particle size distribution. In the equations, *M(R<r)* is the total mass of the particles with size *R* smaller than *r*, which is the sieve size opening; M_T is the total mass of particles; r_L is the maximum particle size as defined by the largest sieve size opening. Logarithmic transformation of Equation 1 results in a linear relationship of the *M(R<r)* and r for D_F (Equation 2).	$\frac{M(R<r)}{M_T} = (\frac{r}{R_L})^{3-D_F}$ $D_F = 3 - m$
Mora et al., 2000	The volume (*V*) is calculated with the particle intermediate axe (*b*), parameter λ and area (*A*). The parameter λ is calculated with the Equation 2. In the Equation 2, *n* is the total number of particles; ρ is the density; *M* is total mass of the particle sample.	$V = \lambda \times b \times A$ $\lambda = \frac{M}{\rho \times \sum_{i=1}^{n}(b \times A)}$
Lanaro, et al., 2001	The particle volume is calculated by the summation of the areas of the cross sections. The particle can be treated as parallel cross sections and the areas of every cross sections can be obtained. After defining the space between the cross sections, the particle volume is calculated by summation of the cross section area times the space. The particle axe can be measured by two geometrical methods as shown in the figure below.	-

	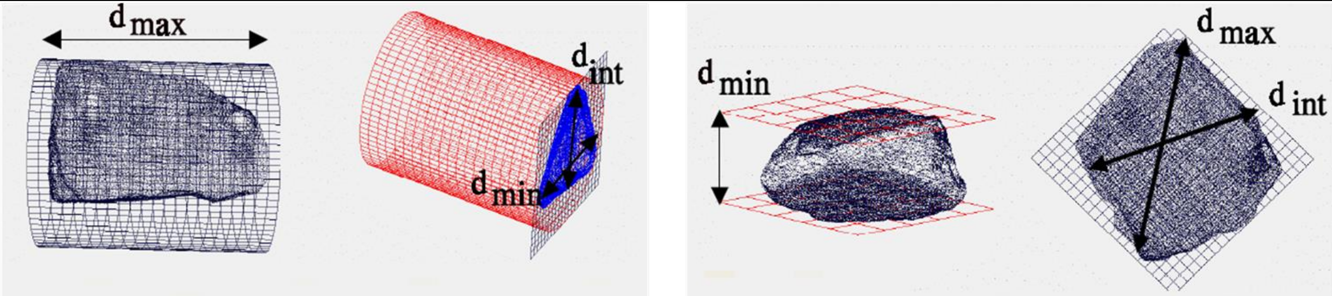 *Two geometrical methods for particle dimension measurement (reproduced from [75])*	
Garboczi et al., 2002	In the Garboczi's method, the surface area is calculated by the derivatives of the spherical harmonic functions. Additionally, the particle volume is computed by the general integral using spherical polar coordinates, which are transformed with the Spherical harmonic.	$V = \frac{1}{3}\int_0^{2\pi}\int_0^{\pi} r^3(\theta,\phi)\sin(\theta)d\theta d\phi$ $S_A = \int_0^{2\pi}\int_0^{\pi} r\left[r_\phi^2 + r_\theta^2 \sin^2(\theta) + r^2 \sin(\theta)\right]^{1/2} d\theta d\phi$
LASS Kim et al., 2002	The volume is calculated by the equation at right side. A pixel corresponds to a volume element in a 3D image (called a voxel) which can be presented by $\Delta x \times \Delta y \times \Delta z$. *H* is the height that is the *Z*-coordinate of the surface point as described at the Table 5 Image analysis systems.	$V = \sum H(\Delta x \times \Delta y \times \Delta z)$
Browne et al., 2002	The size method takes the particle length as the particle size. Thee shape method takes the equivalent diameter as the particle size. The equivalent diameter is the diameter of the circle that has the same particle area.	-
UIAIA Tutumluer et al., 2005 [42]	The surface area is measured through the three orthogonal views of the particle. The 3D reconstruction of the particle is accomplished based on three orthogonal images, when all the voxels are in the 3D framework. Afterwards, the surface area of the particle is computed as the summation of the 2D area elements forming the surface voxels [136]. The volume of the rectangular box is considered as the particle volume, however, the average absolute error is at 11.5% as reported in [42].	$V = abc$

	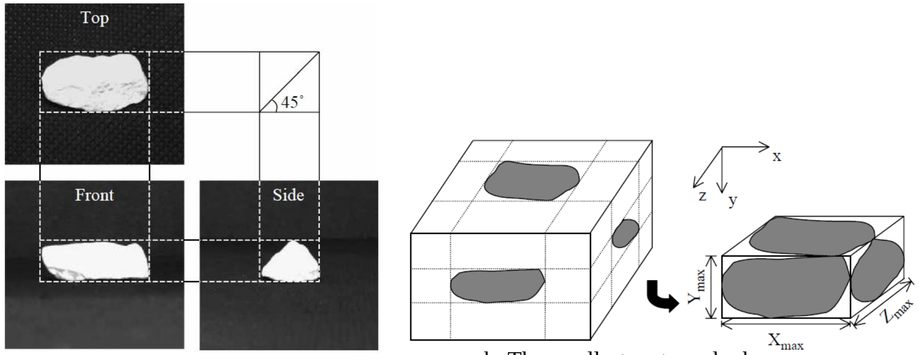 a. Three orthogonal views of a particle b. The smallest rectangular box *Each view of the 3 cameras for one particle (front, top, and side) and the box (framework) for dimension determination (figure reproduced from [136])*	
Descantes, et al., 2006	The particle width is utilised for calculating the PSD curve. The particle volume is assumed as the ellipsoid that is created by revolving the ellipse around its major axis. The longest particle axe (length) is obtained and treated as the major axis of an equivalent ellipse.	-
Anochie-Boateng et al., 2012, 2013	The particle surface area (SA_T) is computed d by summing up all the poly-face surface areas that constitute the particle. The tetrahedrons that constitute the particle can be treated as four vertices $a = (a_1, a_2, a_3)$; $b = (b_1, b_2, b_3)$; $c = (c_1, c_2, c_3)$; $d = (d_1, d_2, d_3)$, and its volume (V) can be calculated with Equation 2. The particle volume is computed with the summation of all the tetrahedrons (Equation 3).	$SA_T = \sum_{i=1}^{n} A_i \quad (1)$ $V = \lvert (a-d)\cdot((b-d)\times(c-d)) \rvert / 6 \quad (2)$ $V_T = \sum_{i=1}^{n} V_i \quad (3)$
PA Ozen & Guler, 2014 [137]	The Equivalent ellipse major axe (E) is expressed as the equation at right side. In the equation: P – the perimeter of particle outline; A – the area of particle outline.	$E = \sqrt{\frac{P^2}{2\pi^2} + \frac{2A}{\pi}} - \sqrt{\frac{P^2}{2\pi^2} - \frac{2A}{\pi}}$

Table 12 Description of degradation evaluation methods

Reference	Description of the degradation procedure	Calculation methods
Tolppanen, 2001 [75]	The LAA test is utilised for deteriorating ballast particles. Four times of laser scanning are performed at the beginning, after 100, 400 and 500 revolutions, respectively. One particle from each sample (7 types in total) is analysed. The Degradation index (DI) is proposed as the average value of the	$DI = 0.5 \times (\Delta F_0 / F_0 + \Delta a / a)$

	roughness change (F_0) percentage and the longest axe (a) change percentage.	
Sekine et al., 2005 [92]	The degradation stages are classified into three levels according to the duration of the LAA tests, i.e. Level 0 (0 min), Level A (10 min) and Level B (35 min). Their morphological indices (i.e. the Angularity index and the Aspect ratio) are obtained using the Fourier series. For ballast particles at each level, 100 particles are photographed and analysed the Aspect ratio and the Angularity index. The distribution of the two morphological indices are compared.	The particle degradation is evaluated by comparing the morphological indices of ballast particles at different LAA test duration.
Fernlund, 2005, 2007	The LAA tests are utilised for obtaining deteriorated ballast particles. Before and after the LAA test, the sample particles are photographed and analysed the three axes of the particles. Afterwards, the PSD change and Flat or elongated ratio change are given for presenting the ballast degradation.	The particle degradation is evaluated by comparing the PSD and the Flat and elongated ratio before and after LAA tests.
Descantes et al., 2006 [122]	The degradation was generated with the micro-Deval milling test (24,000 cycles) until the 2% mass loss is represented. The average Angularity indices of the sample at different stages are presented. The morphological indices (in 2D) of the testing sample are acquired with the VDG40 videograder, including the Angularity index and the Roughness. The different degradation stages are defined based on the micro-Deval abrasion value (5%, 10%, 15%). The results show that the VDG40 videograder can obtain the particle angularity efficiently and accurately.	The results are repeatable with the variation less than 1.5% for Angularity index change.
AIMS Mahmoud et al., 2007	Six different kinds of materials are performed with the micro-Deval polishing for the duration at 15, 30, 45, 60, 75, 90, 105, and 180 mins. The Surface texture index and the Angularity index of particle samples is measured with the AIMS before and after the micro-Deval tests [93]. Another study focuses on the effectiveness of both E-UIAIA and AIM2 on capturing morphology change (form, angularity and surface texture) [39]. The micro-Deval tests are performed on the 11 particle materials with the duration at 15, 30, 45, 60, 75, 90, 105, 180, or 210 mins. The image analysis results are utilised for regression-based statistical model development to determine particle polishing and degradation trends with the consideration of both rate and magnitude of morphology changes.	Surface texture index change; Angularity index change and correlated it with the weight loss. The form change is presented by Flat or elongated ratio change or the Sphericity change.
Okonta et al., 2015 [61]	The LAA test is utilised to create deteriorated ballast at different stages, and the stages are defined based on the machine revolutions (500/1000/1500/2000). The values of the morphological indices at different degradation stages are compared with the initial values to quantify degradation. The abrasion degree decreased as the Roundness increases. The relative ballast fouling ratio can better predict the ballast fouling than the Fouling index, which is concluded by correlating them with the sample roundness changes.	Roundness change and correlated it with the ballast fouling.
UIAIA Qian et al., 2017	The different degradation stages are defined according to the different revolutions in LAA tests (250/500/750/1000/1250/1500/1750/2000). The morphological indices change (AI, F&E, STI and Vol) are used for the degradation evaluation, and the distribution of the ballast samples are given to show the change [91].	Morphological indices change, and correlated with the ballast fouling
Tunkin & Denis, 2014 [45]	The micro-Deval test is used to generate deteriorated particles rapidly. The samples (10 kg) are abraded twice with the same settings, including no steel balls and 100 rpm for three hours. 3D degradation evaluation method can be developed by reconstructing 2D images. For example, in, fifteen 2D images of one particle are reconstructed into one 3D image for degradation evaluation. Degradation is illustrated with the voxels lost, and evaluated by the change of the morphological	The morphological indices include several methods, especially for the surface texture change (details at Chapter 9).

	indices of Form index and Angularity index, obtained with the Spherical harmonics series. As shown in figures below, for comparing particles after each abrasion cycle, it is required to match the particle images in order that the orientation and their centres are the same. Comparing the images before and after abrasion respectively, the difference of the two images can be observed. Difference addition is adding the abraded part to the images after the first cycle of abrasion. The abraded parts are presented in 3D view.	
	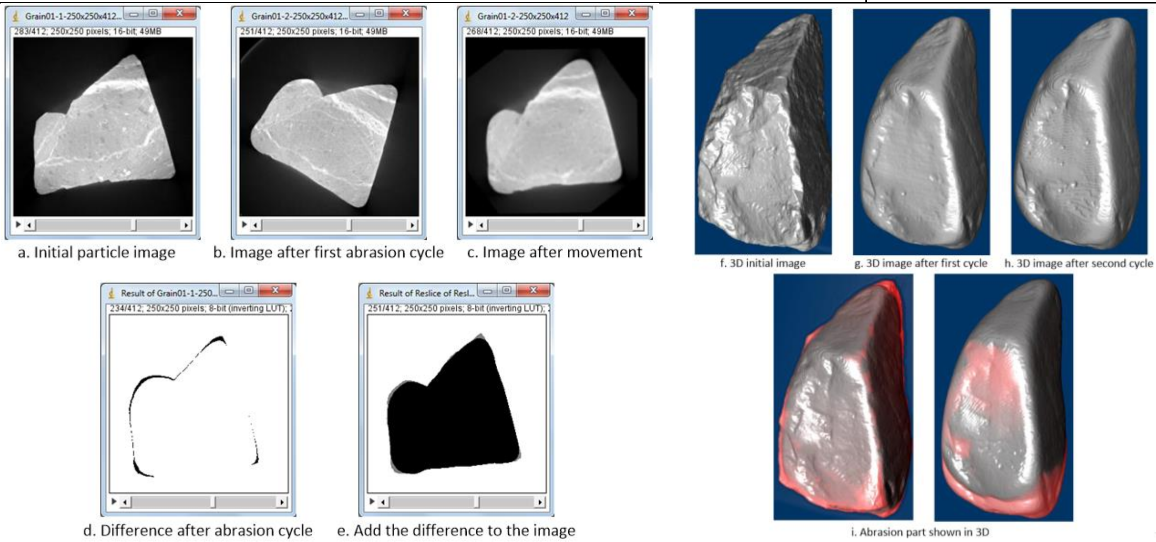 *Example for the procedure explanation of degradation evaluation (modified after [45])*	
Guo et al., 2018	The LAA tests are performed to generate deteriorated ballast particles. By comparing the 3D images before and after the LAA test, the results can be obtained, shown in the figure below. The Abrasion Depth is defined as the value difference of each point at the particle surface. Average Abrasion Depth (AAD) is calculated by averaging the summation of all the Abrasion Depth of one ballast particle. The Maximum Abrasion Depth (MAD) is the maximum value of the Abrasion Depth. More importantly, the breakage is evaluated by the broken number percentage.	Sphericity change, AAD, MAD for degradation evaluation; the AAD correlates well with the LAA loss value.

	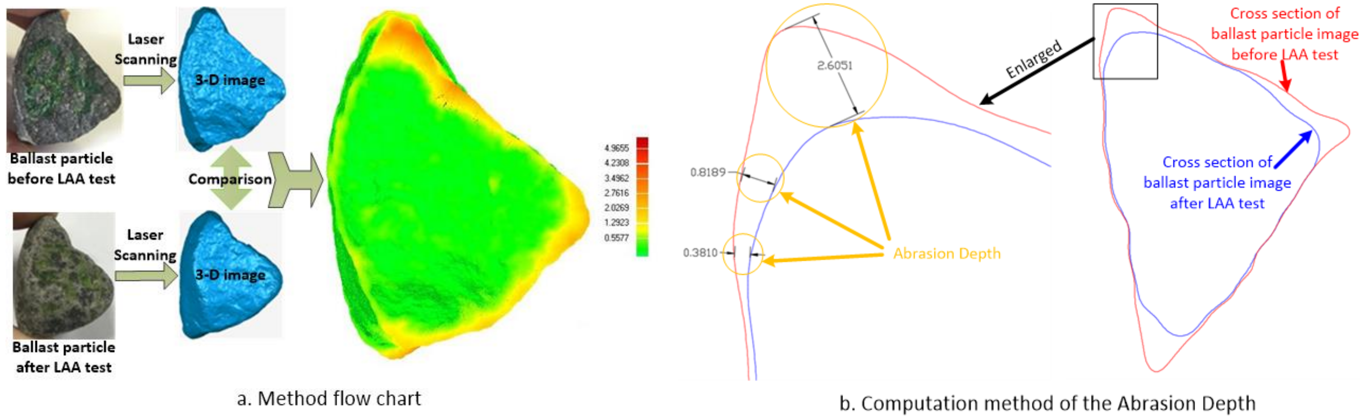 a. Method flow chart b. Computation method of the Abrasion Depth *Method flow chart and the computation method of the Abrasion Depth (modified after [20])*

1170

1171